iScience

Article

Bacteriophage uptake by mammalian cell layers represents a potential sink that may impact phage therapy

Plasma membrane
Nucleus
Phage DNA
Microscopy

Cell lines

10 um

Static & Flow conditions

Phage size

Intracellular phages

Marion C. Bichet,
Wai Hoe Chin,
William
Richards, ...,
Nicolas Hans
Voelcker, Ruzeen
Patwa, Jeremy J.
Barr

jeremy.barr@monash.edu

Highlights

Live-cell imaging showed
that bacteriophages were
internalized by epithelial
cells

Cell type, phage size, and
morphology all influenced
the rate of uptake

Internalized phages were
functional and
accumulated within cells
over time

A pharmacokinetic model
demonstrated the impact
of phage accumulation by
the body

iScience

Article

Bacteriophage uptake by mammalian cell layers represents a potential sink that may impact phage therapy

Marion C. Bichet,[1] Wai Hoe Chin,[1] William Richards,[1] Yu-Wei Lin,[2] Laura Avellaneda-Franco,[1] Catherine A. Hernandez,[3] Arianna Oddo,[4,5] Oleksandr Chernyavskiy,[6] Volker Hilsenstein,[6] Adrian Neild,[7] Jian Li,[2] Nicolas Hans Voelcker,[4,5,8] Ruzeen Patwa,[1] and Jeremy J. Barr[1,9,*]

SUMMARY

It is increasingly apparent that bacteriophages, viruses that infect bacteria and more commonly referred to as simply phages, have tropisms outside their bacterial hosts. Using live tissue culture cell imaging, we demonstrate that cell type, phage size, and morphology play a major role in phage internalization. Uptake was validated under physiological conditions using a microfluidic device. Phages adhered to mammalian tissues, with adherent phages being subsequently internalized by macropinocytosis, with functional phages accumulating intracellularly. We incorporated these results into a pharmacokinetic model demonstrating the potential impact of phage accumulation by cell layers, which represents a potential sink for circulating phages in the body. During phage therapy, high doses of phages are directly administered to a patient in order to treat a bacterial infection, thereby facilitating broad interactions between phages and mammalian cells. Understanding these interactions will have important implications on innate immune responses, phage pharmacokinetics, and the efficacy of phage therapy.

INTRODUCTION

Phages, short for bacteriophages, are viruses that infect bacteria and are the most abundant life form on the planet (Rohwer, 2003; Hatfull, 2015; Rohwer and Segall, 2015). Phages are found ubiquitously in the environment and are a major contributor to global microbial genetic diversity (Breitbart et al., 2003; Clokie et al., 2011; Manrique et al., 2016). Our bodies harbor large numbers of phages, and, together with their bacterial hosts, they constitute a key component of our gut microbiome (Shkoporov and Hill, 2019). The gut carries the largest aggregation of phages in the body, with an estimated 2×10^{12} phages present in the average human colon (Clokie et al., 2011; Sender et al., 2016; Nguyen et al., 2017). These phages are constantly interacting with gut bacteria, as well as the epithelial tissues of the gut (Barr, 2017). Phages are detected in the circulatory systems of the body, suggesting they are capable of translocating from the gut and penetrating throughout the body (Górski et al., 2006; Nguyen et al., 2017). Once past the gut barrier, phages are able to penetrate tissues and major organs of the body, being found in classically sterile regions such as the blood, serum, organs, and even the brain (Geier et al., 1973; Gorski et al., 2003; Srivastava et al., 2004; Dabrowska et al., 2005; Górski et al., 2006; Dor-On and Solomon, 2015; Barr, 2017; Międzybrodzki et al., 2017; Nguyen et al., 2017; Ghose et al., 2019; Huh et al., 2019). Numerous mechanisms pertaining to the transport of phages across epithelial barriers have been proposed (Dabrowska et al., 2005; Górski et al., 2006), including the "leaky gut" where phages bypass cell barriers at sites of damage and inflammation (Handley et al., 2013; Karimi et al., 2016) and receptor-mediated endocytosis (Tao et al., 2013; Lehti et al., 2017). Recently, a non-specific mechanism for phage uptake and transport across epithelial cell layers was proposed by Nguyen and colleagues, whereby epithelial cells uptake phages via macropinocytosis and preferentially transcytose phages from the apical surface toward the basolateral side of the cell (Nguyen et al., 2017). Macropinocytosis is a broad mechanism describing the enclosure of media within ruffles in cells' membrane (Kerr and Teasdale, 2009), prior to internalizing the media, and any phages it may contain, within the cells. Despite their prevalence in the human body, phage's capacity to interact with and influence mammalian cells remains largely unknown. These interactions can have important implications during phage therapy.

[1]School of Biological Sciences, Monash University, Clayton Campus, 25 Rainforest Walk, Clayton, VIC, 3800, Australia

[2]Biomedicine Discovery Institute and Department of Microbiology, Monash University, Clayton, VIC, Australia

[3]Department of Integrative Biology, University of California, Berkeley, Berkeley, CA, USA

[4]Faculty of Pharmacy and Pharmaceutical Sciences, Monash University, Parkville Campus, Parkville, VIC, 3800, Australia

[5]Melbourne Centre for Nanofabrication, Victorian Node of the Australian National Fabrication Facility, Clayton, VIC, 3168, Australia

[6]Monash Micro Imaging, Monash University, Clayton Campus, Clayton, VIC, 3800, Australia

[7]Department of Mechanical and Aerospace Engineering, Monash University, Clayton Campus, Clayton, VIC 3800, Australia

[8]Commonwealth Scientific and Industrial Research Organisation (CSIRO), Clayton, VIC 3168, Australia

[9]Lead contact

*Correspondence: jeremy.barr@monash.edu

https://doi.org/10.1016/j.isci.2021.102287

Phage therapy is a promising alternative to treat antibiotic-resistant bacterial infections. In Eastern Europe, phage therapy has been widely used since its discovery in 1917 (Rohwer and Segall, 2015), whereas in Western countries, phage therapy was largely abandoned in favor of antibiotics (Merril et al., 2003; Kutter et al., 2010; Abedon et al., 2011; Gordillo Altamirano and Barr, 2019). However, with the rise of antimicrobial resistance as one of the greatest threats to human health, phage therapy is being re-established as a potential treatment option for difficult-to-treat, antibiotic-resistant, bacterial infections (Gordillo Altamirano and Barr, 2019). Phages can be administered to patients by a number of routes, including intravenous (IV) or intraperitoneal to treat septicemia; orally to treat gastrointestinal infections; intranasal or inhalation to treat respiratory infections; or topically for cutaneous infections (Dąbrowska, 2019; Matsuzaki and Uchiyama, 2019). The administration route and bioavailability of phages needs to be carefully taken into account in order to achieve favorable efficacy *in vivo*.

In contrast to conventional drugs, phages are unique therapeutic agents capable of self-replicating and maintaining titers in the body (Payne and Jansen, 2000, 2001; Dąbrowska, 2019; Dąbrowska and Abedon, 2019). As such, there is a lack of knowledge regarding phage pharmacokinetics and pharmacodynamics (Dąbrowska and Abedon, 2019). Following administration, two major pharmacokinetic factors important for the efficacy of phage therapy are accessibility and clearance. First, natural barriers such as tissues and mucus layers can decrease accessibility of phages to sites of infection, thereby necessitating the administration of higher doses to achieve a favorable therapeutic effect. Second, phage clearance has been reported to occur rapidly: sometimes within just minutes to hours following parenteral administration in animal models and patients (Keller and Engley, 1958; Hildebrand and Wolochow, 1962; Hoffmann, 1965; Geier et al., 1973; Hodyra-Stefaniak et al., 2019; Sweere et al., 2019; Doub et al., 2020; Lin et al., 2020). Phage clearance within the body is thought to be mediated by three main components: (1) phagocytic cells (Carroll-Portillo and Lin, 2019), (2) the mononuclear phagocyte system (MPS; which was also previously called the reticuloendothelial system or RES), which includes the liver and spleen that filter out and remove phages from circulation (Van Belleghem et al., 2019), and (3) phage neutralizing antibodies, although it is still unclear how effective and rapidly produced these anti-phage antibodies are (Hodyra-Stefaniak et al., 2015; Dąbrowska and Abedon, 2019). Due to these complications, it is difficult to predict how phages will behave in the body when administered and ultimately whether phage therapy will be successful.

One underexplored aspect of phage therapy is the non-specific interactions between phages and tissues. During therapy, large quantities of phage cocktails, which may contain a mixture of complementary phages capable of infecting a certain bacterial species, are administered to patients in order to maintain a killing titer to combat a bacterial infection. Once within the body, these phages can have very short half-lives and are actively removed or inactivated by the body (Hodyra-Stefaniak et al., 2019; Sweere et al., 2019; Doub et al., 2020; Y.-W. Lin et al., 2020). Following phage administration to the body, epithelial and endothelial tissues are among the first and most abundant phage-mammalian interactions. Here, we present new insights into phage-mammalian cell adherence, uptake, and trafficking, via *in vitro* tissue culture. Our results suggest that tissues represent an unaccounted sink for exogenously administered phages. Put within the context of phage therapy, the interaction between mammalian cells and exogenous phages may have important implications for phage administration, dosing, and pharmacokinetics.

RESULTS

The rate of phage uptake varies depending on the cell type

To better understand phage-eukaryote interactions, we used seven *in vitro* tissue culture cell lines that were selected to be broadly representative of different tissues types within the body and examined their interactions with ultrapure, high-titer monocultures of T4 phage. T4 phage is a virulent *Myoviridae* that infect *Escherichia coli* bacterial host. Using real-time live-cell imaging on a confocal microscope with a sensitive hybrid detector, we visualized the interaction and subsequent internalization of phage particles within mammalian cells. Cells were first grown on glass bottom slides for 2 days to generate an ~80% confluent cell layer, followed by fluorescence staining of the nucleus and plasma membrane and maintained in a low feeding state (1% fetal bovine serum for all microscopy experiments). T4 phages were prepared using the Phage-on-Tap method (Bonilla et al., 2016), labeled using SYBR-Gold, subsequently washed to remove residual stain, and then directly applied to the cells and observed using live cell imaging.

Phages were visualized in real time being engulfed and trafficked through all seven of the different cell lines over a 2-hr period (Figure 1A and Videos S1, S2, S3, S4, S5, S6, and S7). The cell types tested include the

CellPress
OPEN ACCESS

Plasma membrane, nucleus, phage DNA
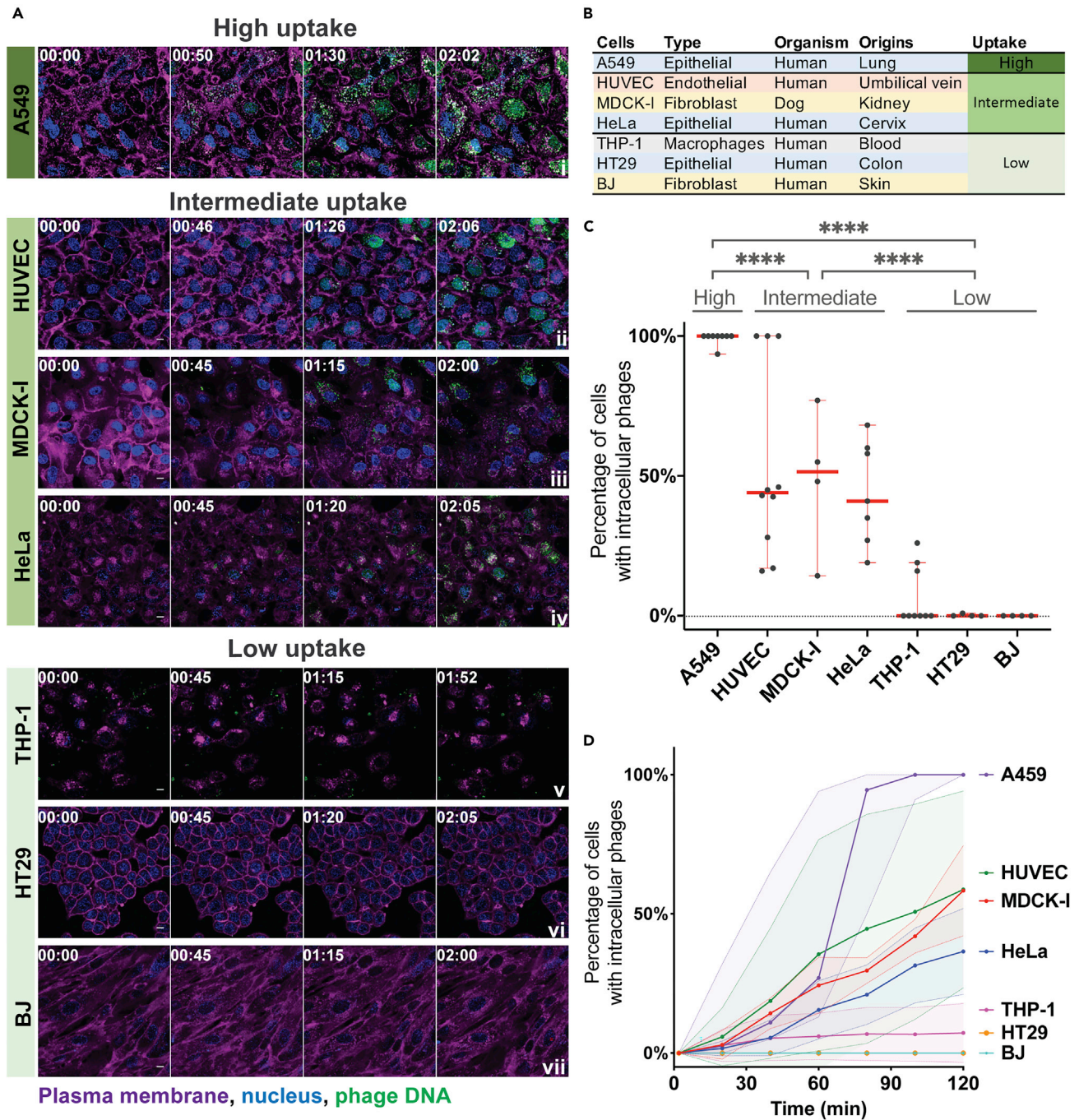
Figure 1. Uptake and internalization of phages varies across cell type

(A) T4 phage was fluorescently labeled, applied to different cell lines, and incubated for 2 hr on a glass bottom slide. Cells were imaged every 2 min using real-time microscopy. Scale bar: 10 μm; timing: hours:minutes.

(B) Table of cell lines used in this study, their cell type, organism, organ origins, and category of uptake. Cells lines are ranked as high, intermediate, and low uptake.

(C) Percentage of cells containing intracellular phages at the 2-hr time point. Scatterplots show medians of percentage of cells with intracellular phages; error bars represent 95% confidence intervals; each dot represents one field of view (FOV). p values between the different groups calculated from a one-way ANOVA, shown as stars (F (2, 43) = 71.23; P < 0.0001: ****).

(D) Percentage of cells containing phages represented across time. For each video, the number of cells with and without intracellular phages in a FOV was manually counted every ten minutes (A549 n = 6; HUVEC n = 8; MDCK-I n = 3; HeLa n = 6; THP-1 n = 8; HT29 n = 3; BJ n = 3). Curve plots show medians of percentage of cells with intracellular phages; the shaded area for each curve represents 95% confidence intervals.

See also Data S1, Figures S1and S2.

following: epithelial cells—HeLa, A549, and HT29, from the cervix, lung, and colon, respectively; fibroblast cells—MDCK-I and BJ, from dog kidney and human skin, respectively; the endothelial cell line—HUVEC from umbilical vein; and monocyte-induced macrophages—THP-1 cells (Figure 1B). The increase in green fluorescence over time corresponds to the uptake and accumulation of fluorescently labeled T4 phages by the cells. We saw the first evidence of phage accumulation within cells occurring around 30 min, with continued accumulation over the following 90 min.

We observed large variation in the uptake of phages across the seven cell types investigated. To quantify this, cells containing intracellular phages were manually counted and compared with the total number of cells in the field of view (FOV) at the 2-hr time point for each replicate. Cells were then categorized as high, intermediate, or low phage-uptake using univariate clustering analysis (Figures 1C and S1) (Wang and Song, 2011). A549 lung epithelial cells showed the highest accumulation of phages, with a median of cells containing fluorescently labeled phages at the 2-hr time point of 99% ($\pm$2%, mean $\pm$ standard deviation [SD]; FOV n = 8; coefficient of variation [CV] = 2%). Next, HUVEC, MDCK-1, and HeLa cells, representing endothelial, fibroblast, and epithelial cell types all showed intermediate levels of phage accumulation at the 2-hr time point, with medians of 44% ($\pm$34% SD; FOV n = 10; CV = 63%), 51% ($\pm$26% SD; FOV n = 4; CV = 54%), and 41% ($\pm$18% SD; FOV n = 7; CV = 42%) of phage-positive cells, respectively. Finally, THP-1, HT29, and BJ cells, representing macrophages, epithelial, and fibroblast cell types all showed little to no accumulation with medians of 0% ($\pm$11% SD; FOV n = 9; CV = 155%), 0% ($\pm$0.5% SD; FOV n = 4; CV = 200%), and 0% ($\pm$0% SD; FOV n = 4; CV = 0%) phage-positive cells at 2 hr, respectively. We further quantified the rate at which cells internalized phages by manually counting the number of cells per frame of interest containing fluorescently labeled phages for each of the FOV per cell lines (Figure 1D). Most cells showed large variability in the uptake rate over the 2-hr period. For A549 cells, which had the highest accumulation of phages, we saw large variation in the rate of uptake, with a median of 27% ($\pm$36% SD; FOV n = 6; CV = 83%) of cells that contained phages at 1 hr of incubation compared to 100% ($\pm$0% SD; FOV n = 6; CV = 0%) of cells at 2 hr. Comparatively, HUVECs, which were classified as intermediate accumulation of phages showed extensive variability in their uptake rates over time, with a median of 12% ($\pm$41% SD, FOV n = 8; CV = 116%) and 46% ($\pm$35% SD; FOV n = 8; CV = 60%) of cells containing phages at 1 and 2 hr, respectively. The rate of entry of SYBR-labeled phages was compared with non-labeled phages and no difference was observed (Figure S2).

To confirm that phages were internalized and not simply attached to the cell surface, we created a three-dimensional (3D) reconstruction using a z stack to visualize the intracellular localization of phages. After the live cell imaging of MDCK-I cells incubated with fluorescently labeled T4 phages for 1 hr (Video S8), we acquired a high-resolution z stack image of one chosen field of view. We reconstituted the 3D volume of the cell to visualize phage repartition in the cytoplasm (Figure 2 top left corner and Video S9). Finally, we looked at the localization of phages in 3D using the XY cross section (Figure 2). The 3D reconstruction of the cell confirmed that phages internalized by the cells (visualized as green fluorescent particles) lie in the same focal plane as the nucleus (Figure 2). Phages were found to be distributed throughout the cell cytoplasm. Additionally, they also appeared to be more abundant within membrane-bound vesicles surrounding the nucleus after the 2-hr incubation.

Phage uptake occurs at comparable rates under both static and flow conditions

The previous experiments were all conducted under static conditions, where phages were directly applied to the cell culture media and phage-cell encounters driven purely by diffusion. However, phages administered to the body encounter dynamic environments and active fluid flow, such as in the circulatory and lymphatic system. These dynamic conditions may lead to increased phage-cell encounter rates or altered cellular uptake (Kim et al., 2007, 2012, 2016; Son, 2007; Navabi et al., 2013; Thuenauer et al., 2014). We investigated whether phage uptake rates under static conditions were comparable with uptake rates under fluid flow and shear conditions that mimic the circulatory systems of the body (Figure 3A). We chose HUVECs to use in our flow experiment for two main reasons: the first being that they are part of the intermediate uptake group as previously shown (Figure 1) and, secondly, are endothelial cells and would be among the first type of cells to be in contact with circulating phages in the human body. Using an in-house fabricated microfluidic device mounted on a glass coverslip adapted for confocal microscopy (Barr et al., 2015; Chin and Barr, 2019), we seeded the device with HUVECs and incubated it under static conditions for 12 hr to ensure sufficient cellular attachment to the substrate. Cells were allowed to settle within the device under a low flow rate of 0.66 μL/min for one day, before increasing to a final flow rate of 8 μL/min until cells
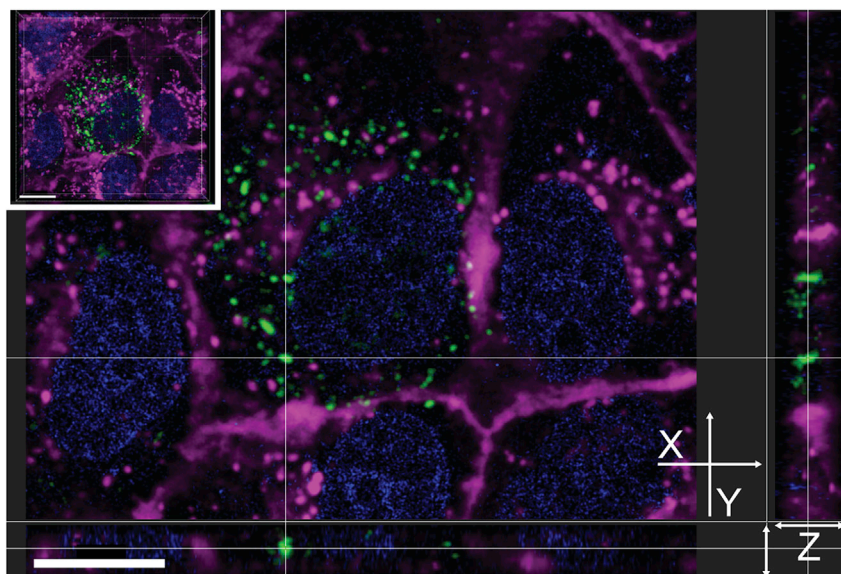
Plasma membrane, nucleus, phage DNA

Figure 2. 3D reconstruction of intracellular phages

MDCK-I cells were incubated for an hour with T4 phages on glass bottom slide before live acquisition of a high-resolution z stack to visualize phage dispersion inside of cells. 3D cell projection is shown in the top left corner. The cross in the center of the image shows a cluster of internalized phages with its Z dimension (depth) represented in the side views. Scale bar: 10 μm.

reached confluency. Physiological shear stress values observed in the human body range from 0.1 dyne/cm^2 in the microcirculation, reaching higher rates of 50 dyne/cm^2 found in larger circulatory vessels (Davies et al., 2005; Park et al., 2011; Wang et al., 2012; Abaci et al., 2014; Yum et al., 2014). Due to the volumes of media and quantity of phages applied to the chip, we chose a flow rate of 8 μL/min, which is equivalent to a shear stress of 0.1 dyne/cm^2 in our chip and was at the lower end of physiological circulatory range (Table S1). We perfused the chips with media containing 10^9 phages/ml, with phage uptake visualized as previously described at 2- and 18-hr time points. Even though the volumes and quantity of phages seen by the cell layers in the static (200 μL) and flow (960 μL) conditions are different, we still observe similar rates of T4 phage uptake after 2 hr (Figures 1A, 3Bii, and S4). Comparatively, after 18-hr incubation under shear stress, we observed a significant increase in the fluorescence intensity compared with 2 hr incubation (unpaired t test, P < 0.001) (Figure S4), suggesting that phage accumulation and saturation within cells continues over longer incubation periods.

Phage type and size effects intracellular uptake

Next, we looked three different phage types with differing sizes and their subsequent rates of cellular uptake. We chose three *Escherichia coli* infecting phages: T4 phage from the *Myoviridae* family, measuring 90 nm wide and 200 nm long with a contractile tail; lambda phage from the *Siphoviridae* family, measuring 60 nm wide and 150 nm long with a non-contractile tail; and T3 phage from the *Podoviridae* family, measuring 55 nm wide and 30 nm long with a small non-contractile tail. We tested these phages against three cell lines representative of high, intermediate, and low rates of uptake (Figure 1C): A549 cells with a high rate of uptake, HUVECs with an intermediate rate, and BJ cells with a low rate. We incubated phages with the cells for 2 hr, acquiring images every 2 min (Videos S1, S2, S7, S10, S11, S12, S13, S14, and S15), with the final time point represented in Figure 4A. The first row of images shows clear differences in T4 phage uptake between the three cell lines (Figure 4A). However, when we applied the lambda and T3 phages to the three cells lines, we saw a large increase in the uptake of both phages compared with T4. This was particularly evident in the BJ cell line, which had effectively no T4 phage update over a 2-hr period but nonetheless demonstrated increased uptake of the smaller sized lambda and T3 phage. We quantified phage uptake across type and size using a pipeline built with CellProfiler software (McQuin et al., 2018) (see transparent methods) to analyze the median gray-value intensity in the cell region (median over all pixels in FOV marked

A

Flow of 0.1 dyne/cm^2
with 10^9 phages per ml

Input

Waste

Output

Glass coverslip

Confocal
Microscope
Objective

B

HUVEC cells
Plasma membrane, nucleus, phage DNA

MERGE

Phage DNA

i- No phages   ii- 2 hours   iii- 18 hours
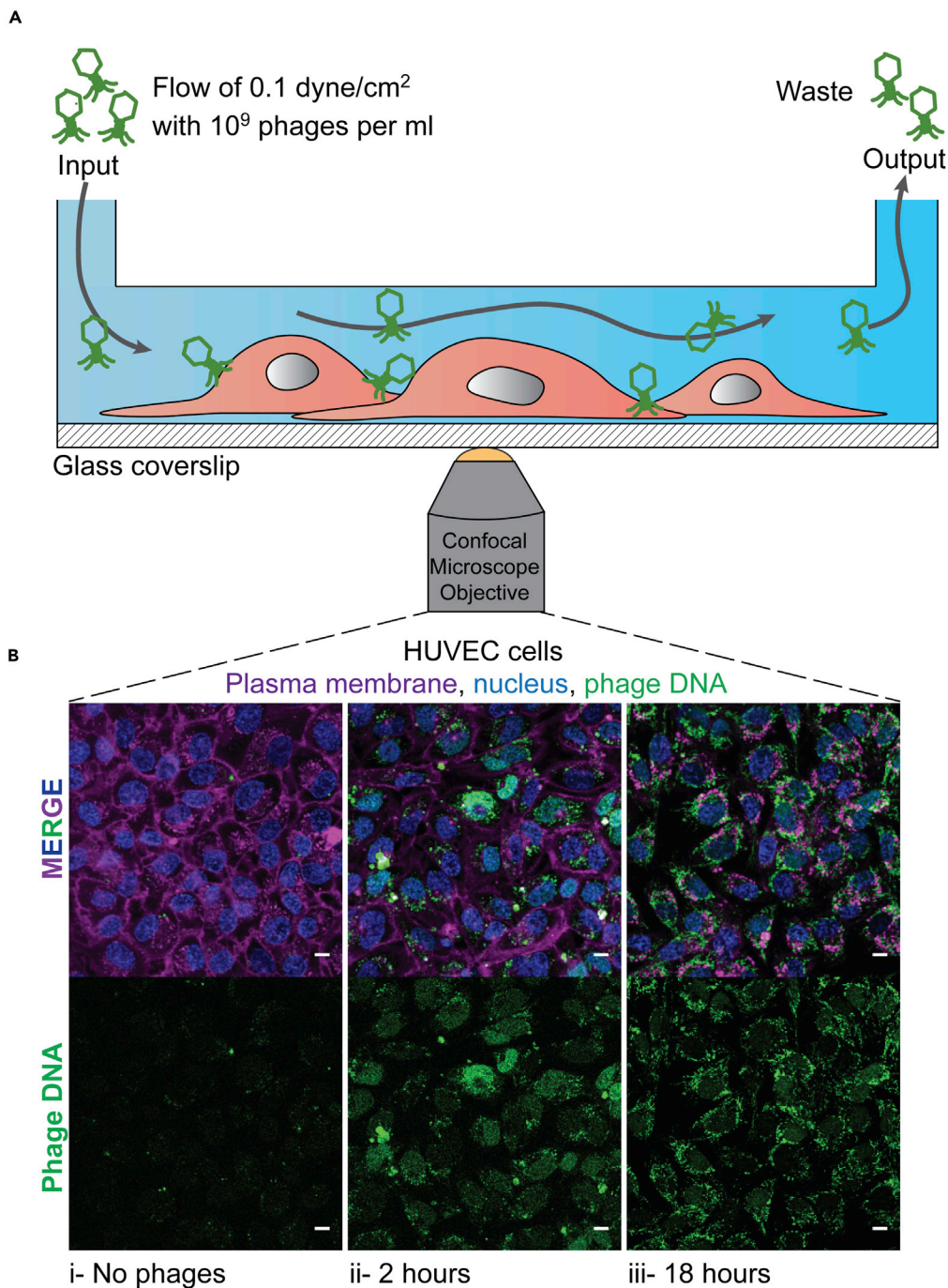
Figure 3. Uptake of phages under fluid flow and shear stress

T4 phage was applied to HUVECs within a microfluidic channel of a microfluidic device under a shear stress for 2 or 18 hr with images collected via real-time microscopy images.

(A) Schematic of the microchannel showing the flow from one port of the channel to the other side of the channel where the waste was collected.

(B) (i) Control cells without phages. Cells incubated under a constant flow of phages at a rate of 8 μL/min for either (ii) 2 or (iii) 18 hr. Scale bar: 10 μm.

See also Figures S3 and S4.
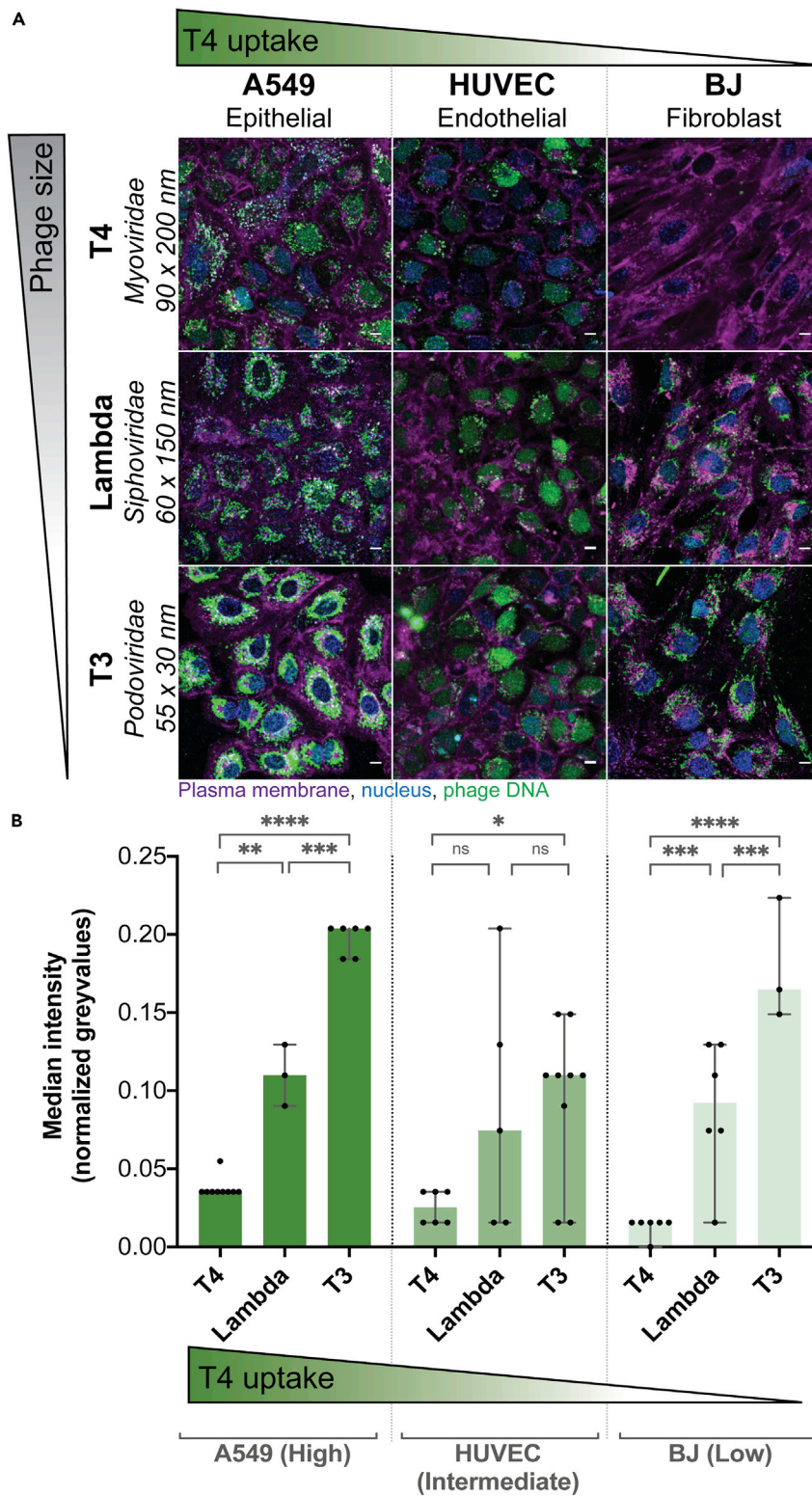
Figure 4. Cellular uptake of differing phage types

Real-time microscopy images showing differential uptake of three phages. One representative cell line from each of the three high, intermediate, and low uptake groups was picked.

Figure 4. Continued

(A) Images were acquired in real time. Green gradient shows the qualitative increase in T4 phage uptake (Figure 1C), while gray gradient shows qualitative decrease in phage size. Scale bar, 10 μm. The image shown is the last image at 2-hr acquisition.

(B) Fluorescence intensity of the "phage object" area in normalized gray values at the 2-hr time point (A549-T4 $n = 9$; A549-lambda $n = 3$; A549-T3 $n = 6$; HUVEC-T4 $n = 6$; HUVEC-lambda $n = 3$; HUVEC-T3 $n = 6$; BJ-T4 $n = 6$; BJ-lambda $n = 6$; BJ-T3 $n = 3$). Scatterplots show medians over all pixels in the cell FOV; error bars represent 95% confidence intervals; each point represents one FOV. p values calculated from a one-way ANOVA (P < 0.0001: ****; p < 0.05: *; ns: non-significant).

as cells) as a proxy for fluorescence intensity of phage (Figure 4). For T3 phage, a *Podoviridae* and the smallest phage of the three tested, we observed the highest rate of uptake across the three cell lines (analysis of variance [ANOVA] one way, F (2, 45) = 71,32; P < 0.0001). This was especially evident for the BJ cell line where the median intensity of the phage fluorescence signal increased from a median of 0.01 normalized gray value with T4 phage (± 0.006 SD; FOV $n = 6$; CV = 49%) up to 0.09 with lambda (± 0.04 SD; FOV $n = 6$; CV = 49%) and finally to 0.16 with T3 phage (± 0.04 SD; FOV $n = 3$; CV = 22%) (Figure 4B). Based on our microscopy results, we suggest that smaller sized phages showed increased rates of cellular uptake, with these effects being more pronounced in our intermediate and low uptake cell lines.

Phages adhere to mammalian cells, resulting in inactivation and uptake

We demonstrate that phages have different rates of cellular uptake depending on both cell type and the size and morphology of phages. Yet whether these phages remained functional or if they were inactivated by the cellular uptake and trafficking pathways remains unclear. To answer this, we quantified the number intracellular phages using two methods: classic plaque formation unit (PFU) assays and droplet digital PCR (ddPCR). Briefly, PFUs allowed us to quantify the number of active or functional phages present within the cells, while ddPCR quantified the absolute number of phage DNA genome copies present in the sample. We evaluated the accuracy of the two techniques with a dilution series of our initial phage sample from 10^9 to 10^2 phages per ml using PFU and ddPCR (Figure S5). Subtracting active phages (PFU) from phage DNA genome copies (ddPCR) enabled us to quantify the proportion of phages inactivated or damaged during cellular uptake and trafficking, as these damaged phages are no longer able to infect their bacterial host and therefore will only be detected by ddPCR.

In order to differentiate between intracellular phages and those adhered to the cell surface, we incubated cells with T4 phages ($\sim 10^9$/mL) for two different periods of time: 30 s, which is too short for phage internalization, as previously observed in the microscopy videos (Figures 1, 3, 4, and S6) where for A549 and HUVEC cells, 10 min is the earliest time point to observe intracellular phages, and 18 hr, to maximize the number of internalized phages. After incubation at each time point, cells were extensively washed to remove non-adherent phages, lysed, and phages quantified by both PFU and ddPCR (Figure 5A). We compared the same representative cell types previously used for high, intermediate, and low uptake cell lines (Figure 5B). For all three cell lines, we saw between 90 and 2200 active phages (PFU)/ml adhered to the cells within 30 s treatment, with a median of 625 PFU/mL (± 420 SD; $n = 6$; CV = 60.1%), 325 phages/ml (± 300 SD; $n = 6$; CV = 76.6%), and 250 phages/ml (± 850 SD; $n = 6$; CV = 114%) for A549, HUVEC, and BJ cells, respectively, suggesting a small, yet persistent number of phages adhere to the cell layer. After 18 hr of incubation, we saw a large increase in the number of functional phages associated with the cells, with between 1.1×10^4 and 3.1×10^6 phages/ml accumulating within the three cell lines. Looking across the different cell lines, we see the highest accumulation of phages in the intermediate uptake cells, with a median of 5×10^5 PFU/mL ($\pm 6.4 \times 10^5$ SD; $n = 9$; CV = 85.7%) followed by the high and low uptake with medians, respectively, of 1.2×10^5 PFU/mL ($\pm 8.4 \times 10^4$ SD; $n = 9$; CV = 65.7%) and 5×10^4 PDU/ml ($\pm 1.4 \times 10^6$ SD; $n = 9$; CV = 144.3%), although there was no significant difference between the three cell lines (P > 0.1, ANOVA one way). We note that the BJ cell line, which showed the lowest rate of uptake observed via microscopy (Figure 1), still accumulated active phages over prolonged periods of time with non-significant differences of active phages at 18 hr observed with two other cell lines (unpaired t test, two tailed, P > 0.08 with A549 and P > 0.6 with HUVEC). This suggests that despite differences in the cells rates of phage uptake, even low uptake cell lines are capable of internalizing phages over extended time periods.

Surprisingly, when looking at ddPCR results, we see an increase in phage DNA associated with the 30 s treatment in all cell lines, with between 3.9×10^2 and 2.7×10^4 DNA genome copies/ml persisting. When quantifying the inactivated phages at 30 s treatment, which was calculated as the difference in DNA genome copies and PFU, we observe between 7×10^1 and 2.7×10^4 inactivated PFU/ml. These results suggest that (1) phages adhere to
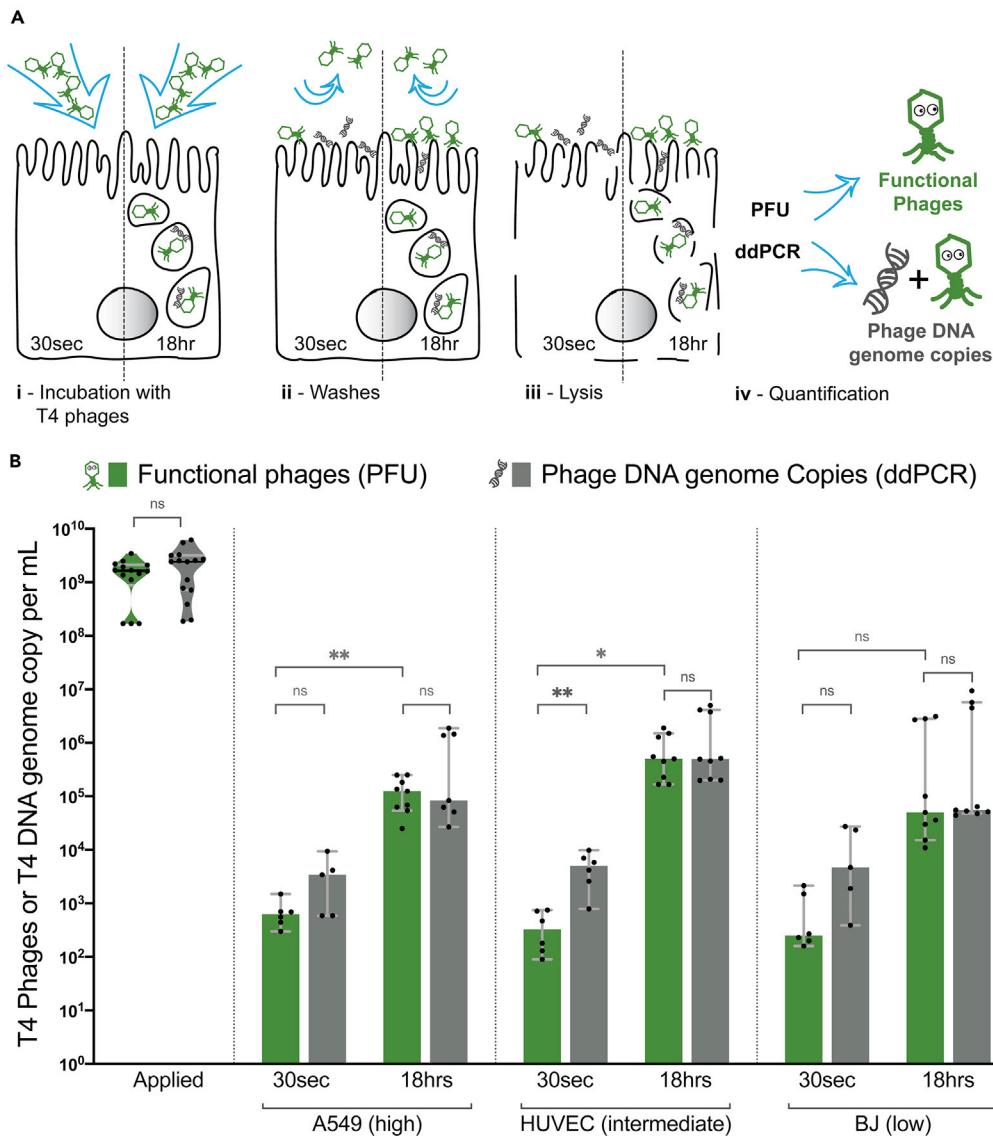
Figure 5. Quantifying adherence and internalization of phages and their activity

(A) Schematic representation of the experiment. T4 phages were applied to cells either 30 s as an adherence control or for 18 hr to saturate phage uptake. Phages were quantified using both traditional plaque assays (PFUs) and digital droplet PCR (ddPCR), across three different cell lines: A549, HUVEC, and BJ, representative of the high, intermediate, or low phage uptake.

(B) Active T4 phages in green quantified by PFU and in gray the total number of phage DNA genome copies per sample quantified by ddPCR, including both active and inactive phages. Scatterplots show medians of phages or DNA genome copies/ml; error bars represent 95% confidence intervals; each point represents one sample. p values calculated from an unpaired t test between each pair (p < 0.001: ***; p < 0.01: **; p < 0.05: *; ns: non-significant).
See also Figures S5–S8 and Tables S1–S3.

mammalian tissues, with a portion of these phages being inactivated, (2) longer incubation time allows for adhered phages to be internalized and accumulate inside of the cells, and (3) the majority of internalized phage particles remain active and stably persist within the cells for up to 18 hr.

Phage inactivation and internalization influences pharmacokinetics

A key underexplored aspect of phage pharmacokinetics (PK) is the non-specific interactions between phages and the epithelial and endothelial tissues. To address this, we integrated our experimental data (Figure 5) with

an established PK model for phage administration in rats (Lin et al., 2020). The model was established from a single-dose PK study performed in healthy rats, following an intravenous bolus of phages. The phage disposition in blood was well characterized using a standard three-compartment PK model (Lin et al., 2020). In order to evaluate the impact of phage inactivation and internalization by mammalian cells on phage distribution, a fourth compartment was added to the existing model, representing the epithelial and endothelial tissues (Figure 6A). Deterministic simulations were subsequently performed with the previously estimated PK parameters (Lin et al., 2020), and the first-order inactivation constant was estimated from our *in vitro* data (ddPCR). Inactivation rate constant was calculated using both the 30 s- and 18 hr-derived constants, as a representative of both the rapid and prolonged phage accumulation in tissues (Figure 6B, Data S2 and S3 and Table S5). Deterministic simulations were performed at an IV bolus dose of 10^9 phages. With the inactivation rate constant calculated using 30 s data, complete removal of phages was noted as short as three hours. This is consistent with the 30 s *in vitro* data, in which rapid inactivation was observed. Comparatively, using the inactivation rate constant calculated using the 18-hr data, an initial rapid decay of circulating phages followed by a longer tail and phage persistence in the blood was observed for up to 32 hr. These two models represent two extremes of rapid and prolonged phage accumulation in tissues, highlighting the potential impact of these cellular mechanisms on phage disposition. Further studies characterizing both the affinity of phage-mammalian interactions and their influence on PK are needed for better clinical translation.

DISCUSSION

Phage therapy is one of the more promising alternatives in the fight against antibiotic resistance (Abedon et al., 2011; Loc-Carrillo and Abedon, 2011; Nilsson, 2014; Gordillo Altamirano and Barr, 2019). However, the effective dosing and administration of phages to the body during phage therapy remains a major challenge. Our understanding of the interactions between bacteriophages and mammalian cells may have important implications for phage therapy. In this article, we investigate the interactions between phages and *in vitro* tissue culture. We demonstrate that cell type plays a major role in the uptake process of phages, with individual cells taking up phages at different rates, even among the same cell types (e.g., epithelial, endothelial, etc.). Uptake rates were validated under shear stress conditions using a microfluidic device that mimics the shear stress to which endothelial cells are exposed to *in situ* (Han et al., 2012; Hosta-Rigau and Städler, 2013), with uptake shown to be comparable to static conditions. Using live cell imaging, we show that phages accumulate within cells over time and that smaller phages are internalized at higher rates than larger phages. Phages were found to adhere to mammalian cells, with adherent phages being internalized by macropinocytosis over the following 18 hr of incubation, with functional phages accumulating and stably persisting within the cells. Finally, we incorporate our results into an established pharmacokinetic (PK) model (Lin et al., 2020), demonstrating the potential impact of phage accumulation by epithelial and endothelial tissues, which represent an unaccounted sink of phages within the body. Our study provides novel insights into the uptake of phages by mammalian cell layers.

The mechanism of non-specific phage uptake by *in vitro* tissue culture cell lines was previously demonstrated to occur via macropinocytosis (Nguyen et al., 2017). We used mostly the same cell types as in the Nguyen study to ensure macropinocytosis was also the main entry way for phages into our cells. Cell types have been reported to have differing basal rates of macropinocytosis depending on their function and location within the body (Kerr and Teasdale, 2009), thereby influencing their rate of phage uptake. We found a high level of heterogeneity regarding phage uptake and internalization across all cell lines in our study (Figure 1). We have verified this finding multiple times and demonstrate that it is specific to neither cell type nor phage. Even though the cells used for microscopy were always a confluent cell layer, it is possible that the cell cycle were not synchronized, thereby contributing to differential uptake rates of phages among the same population of cells. Further, the mucus layer is known to interact with phages (Barr et al., 2013, 2015) and may play a role in the heterogeneity of phage uptake. Most of the cell lines used were non-mucus producing cells. However, we did test the effect of phage internalization on two mucus producing cell lines: A549s, which are a lung epithelial cell line that produce a thin mucus lining, and HT29s, which are a colonic epithelial cell line that produce a thicker mucus layer. A549s had the highest level of phage internalization, while HT29s with their significantly thicker mucosa had minimal phage internalization over a 2-hr period (Figure 1). Thus, it is likely that thicker mucus layer reduced the number of phages that were in contact with the cell membrane, thereby decreasing phage internalization.

The macropinosome plays an important role in the presentation of antigens for pattern recognition receptors located in other organelles and in the activation of innate immune responses (Canton, 2018). It is clear
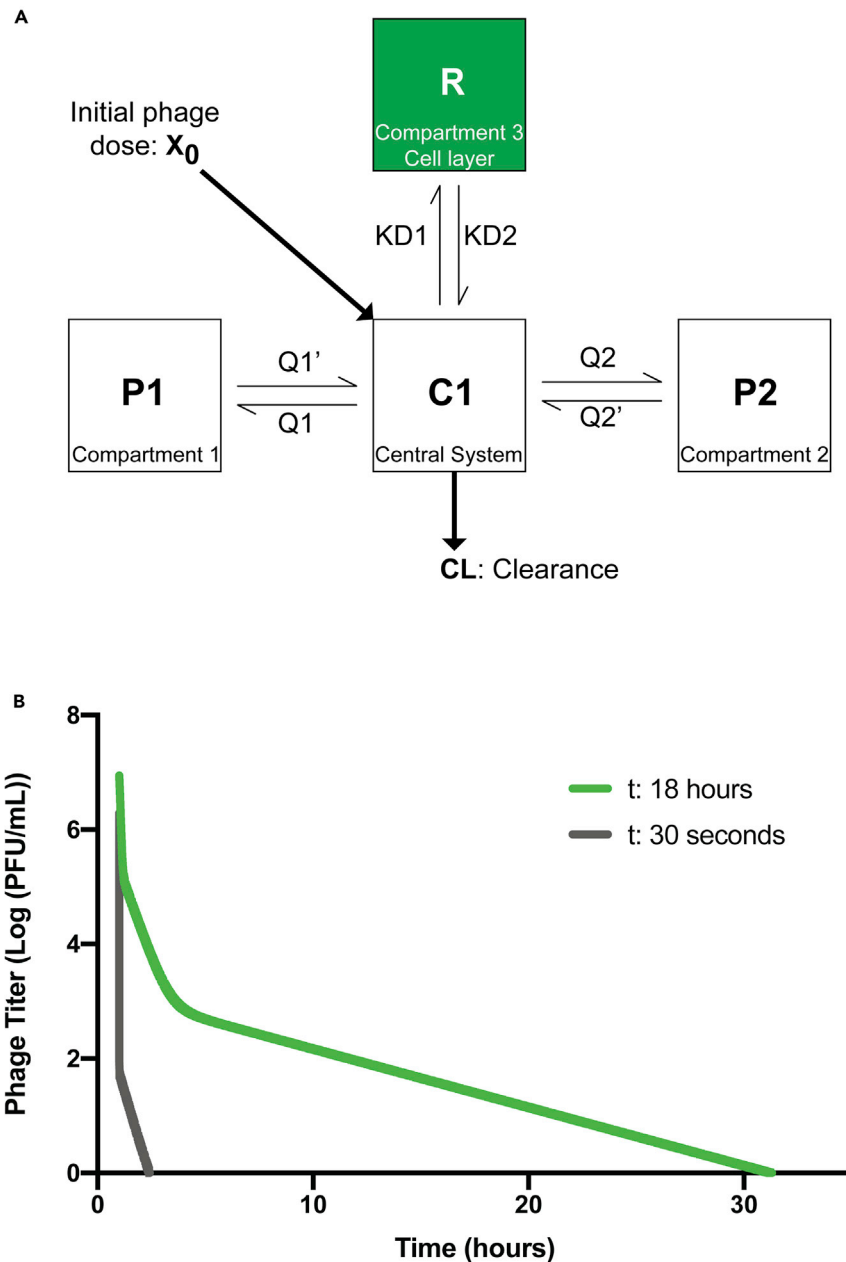
Figure 6. Pharmacokinetic (PK) model of inactivation and internalization of phages by mammalian tissues

(A) Schematic of the standard 3-compartment model with an additional inactivation compartment. X_0, the initial dose of phages and CL phage total body clearance. C1, the central compartment representing the central system (*i.e.*, the blood). P1 and P2 compartments represent various organs or tissues participating in phage decay. R, the new compartment representing *in vitro* cell layers as a potential sink of phages. Q1 and Q2 are intercompartmental clearance one and two, respectively. KD1 is the first-order inactivation constant, and KD2 is the first-order reactivation constant (assumed to be zero in our model).

(B) Graph representing the decay of phages per central volume of distribution over time calculated with *in vitro* data. First order for the 30 s graph is 1511 1/h/rat, and for the 18 hr, the first order is 0.44 1/h/rat (calculation in Table S5).

See also Codes Data S2 and S3 and Table S5.

that labeled phages accumulate within the macropinosomes over time, but whether they were subsequently degraded by the endosomal/lysosomal system or recycled and fused back with the plasma membrane remains to be investigated (Kerr and Teasdale, 2009). Here, we propose that phages that come in

contact with mammalian tissue layers can interact with and adhere to the cell membrane. This adherence leads to an internalization of membrane-associated phages via non-specific macropinocytosis, which allows for the steady accumulation of phages within the cell over time. Following phage uptake by mammalian tissues, the fate of internalized phages is multifaceted and has been demonstrated to include; phage inactivation by the cell (Geier et al., 1975) transcytosis and secretion of active phages on contralateral cell layers (Nguyen et al., 2017), dissemination of phages throughout the body (Ghose et al., 2019), and inactivation of phages by innate immunity (Sweere et al., 2019). Further research is required to probe the specific mechanisms of phage adherence, uptake, and the cellular mechanisms that govern the trafficking of phages within cells (Talman et al., 2019; Bodner et al., 2020).

Using three different phages, from different families, with different sizes, we were able to show an effect of phage morphology and size on the rate of uptake across three different cell lines. Using real-time microscopy, we demonstrate that the smaller sized *Podoviridae* phage particles had increased rates of uptake, especially in low uptake cell lines. One hypothesis for the increased uptake of these smaller sized phages may simply be the result of an increased number of particles capable of interacting with actin-mediated ruffles associated with of macropinosome formation, thereby leading to a higher number of phages engulfed within each macropinosome (Swanson and Watts, 1995; Kerr and Teasdale, 2009). It is also possible that there is a difference in ruffle size across cell lines leading to a predisposition of some cells to uptake differently shaped and sized phages. A similar relationship between particle size and uptake has been made with nanoparticles, where it was observed that 50-nm sized nanoparticles had high rates of uptake, which coincidentally are of similar size as our T3 phages (Yin Win and Feng, 2005; Lu et al., 2009; Zhu et al., 2013). It was also shown that the cell type as well as the particles shape influenced uptake, with disc-shaped particles having higher rates of uptake compared with elongated rod shapes. Again, our T3 phages are coincidentally similarly shaped to the disc-shaped particles (Agarwal et al., 2013; Hsiao et al., 2014), indicating that the shape of phages may play a role in their uptake: a factor that we cannot rule out from our study. It is intriguing to speculate that much of the research into nanoparticle delivery has converged upon parameters analogous with biology's own naturally occurring nanoparticles: the bacteriophages.

We observed that following the adsorption of phages with *in vitro* cell culture layers, a high proportion of phages were inactivated (Figure 5B): a phenomenon which, to our knowledge, has not been previously reported. Our first hypothesis to explain this rapid inactivation is that upon interaction with cell surface features, phages are mechanically triggered to eject their genomes, thereby leading to inactivation (Kellermayer et al., 2018). This would implicate an increase of phage DNA at the cell surface, which we observed via ddPCR results, along with a concomitant decrease in functional phage particles. Another hypothesis is that the transient and non-specific interactions between the phages and the cell surface features, including glycoproteins, glycolipids, and mucins (Barr et al., 2013), may physically block or impede the phage such that it is unable to access its host bacterial receptor for plaque quantification, thereby only being detected via ddPCR. Finally, this inactivation could be the result of the degradation of the phage capsid due to enzymes, secretions, or cellular products; though our negative controls show this is unlikely as there was no effect of spent cell culture media on phage infectivity (Figure S7). At this stage, while we cannot conclude the specific mechanisms inducing this loss of phage viability, our results suggest that this inactivation and adsorption to the tissue may represent a potential sink for circulating phages in the body. In a healthy gut microbiome, phages play a major role in controlling the bacterial population. The gut epithelium likely influences phage abundances in the gut via these same uptake and inactivation mechanisms, which could further impact the gut microbiome and its disease states (Gogokhia et al., 2019).

During phage therapy, the cells, tissues, organs, and systems of the body play an important role in the efficacy of treatment due to their effect on the sequestration of active phages and subsequently limiting accessibility of phages to the site of infection (Dąbrowska, 2019; Dąbrowska and Abedon, 2019). It has been proposed that the MPS is primarily responsible for the filtering and removal of the phages during phage therapy, with the liver and spleen considered the main organs responsible for filtering out circulating phages (Geier et al., 1973; Merril et al., 1996; Hodyra-Stefaniak et al., 2015). Recent case studies of phage PK following IV administration have shown rapid clearance in both humans and animal models, with over >99% of phages applied removed from circulation within the first few hours (Schooley et al., 2017; Y.-W. Lin et al., 2020). In a literature review, Dąbrowska (2019) noted that the phage titers in the blood immediately following intravenous injection (1–5 min) were markedly less than the expected hypothetical dilutions. Even when accounting for phage dilutions in the blood or total body volume, phage titers only

reached between 0.02% and 0.4% of their predicted titers. This suggests that there is significant and rapid uptake of phages by the organs and cells of the MPS or alternatively the sequestration of phages by epithelial and endothelial tissues. All of the cell lines that were used in this study, including; endothelial, epithelial, macrophages, or fibroblast, may be in contact with phages at any time during therapy. Our results demonstrate that phages adhered to and were subsequently internalized by these cells (Figure 5B). The model we developed in this study (Figure 6), while preliminary, illustrated the potential impact that tissues play on the inactivation of phages following their delivery to a patient, with phages most likely displaying non-linear PK (in addition to non-linear clearance). We suggest that cell layers are a potential sink for phages and that these interactions may have unrecognized consequences on phage dosing and PK during treatment. Further research investigating the potential interactions between phages and mammalian tissues and cell layers *in vivo* is needed.

Limitations of the study

Our study describes the uptake of bacteriophages by mammalian tissues and applies these findings toward the administration of phages to the body. However, there are a number of important limitations and caveats to our study. Firstly, our study has been conducted using *in vitro* tissue culture cell lines and does not include any primary cell lines or *in vivo* animal models. Conducting *in vivo* animal models to investigate the non-specific uptake of phages by epithelial and endothelial tissues is challenging. Treating animals with phages intravenously, which is one common way of administering phages to a patient, has been done many times in prior literature (Keller and Engley, 1958; Geier et al., 1973; Hodyra-Stefaniak et al., 2015; Lin et al., 2020). However, the removal/inactivation of administered phages by the animals does not directly relate to our proposed epithelial and endothelial uptake mechanism, with additional intertwined phage removal mechanisms also at play, including phagocytic cells, MPS system, and adaptive immune response. As an alternative to *in vivo* models, we report data using a microfluidic model system and a phage PK model. Further *in vivo* studies are needed to investigate the influence of phage uptake by mammalian tissues and its impact on phage therapy.

We also described an effect between different phages, with varying size and morphology, and their subsequent uptake by mammalian cells, with smaller sized phages being internalized at higher numbers. We demonstrated this using three model *E. coli* phages: T4, lambda, and T3 phage, representing a large, medium, and smaller sized phage. Even though the phages used here are from different families, they are all dsDNA *Caudovirales* infecting *E. coli* strains. It is important to note that we have not tested other phage types, such as ssDNA, RNA, or filamentous phages, which could lead to different results. Further, phage size is only one potential factor likely influencing mammalian uptake rates. Additional phages and their associated physical parameters, including size, morphology, host range, and capsid proteins, along with representative nanoparticles, need to be investigated to confirm this observation.

Resource availability

Lead contact

Jeremy J. Barr.

Materials availability

This study did not generate any unique materials.

Data and code availability

This study did not create any data or code that was not already available.

METHODS

All methods can be found in the accompanying transparent methods supplemental file.

SUPPLEMENTAL INFORMATION

Supplemental information can be found online at https://doi.org/10.1016/j.isci.2021.102287.

ACKNOWLEDGMENTS

AUTHOR CONTRIBUTIONS

DECLARATION OF INTERESTS

REFERENCES

Abaci, H.E., Shen, Y.I., Tan, S., and Gerecht, S. (2014). Recapitulating physiological and pathological shear stress and oxygen to model vasculature in health and disease. Sci. Rep. 4, 1–9.

Abedon, S.T., Kuhl, S.J., Blasdel, B.G., and Kutter, E.M. (2011). Phage treatment of human infections. Bacteriophage 1, 66–85.

Agarwal, R., Singh, V., Jurney, P., Shi, L., Sreenivasan, S.V., and Roy, K. (2013). Mammalian cells preferentially internalize hydrogel nanodiscs over nanorods and use shape-specific uptake mechanisms. Proc. Natl. Acad. Sci. U S A 110, 17247–17252.

Barr, J.J., Auro, R., Furlan, M., Whiteson, K.L., Erb, M.L., Pogliano, J., Stotland, A., Wolkowicz, R., Cutting, A.S., Doran, K.S., et al. (2013). Bacteriophage adhering to mucus provide a non-host-derived immunity. Proc. Natl. Acad. Sci. U S A 110, 10771–10776.

Barr, J.J., Auro, R., Sam-Soon, N., Kassegne, S., Peters, G., Bonilla, N., Hatay, M., Mourtada, S., Bailey, B., Youle, M., et al. (2015). Subdiffusive motion of bacteriophage in mucosal surfaces increases the frequency of bacterial encounters. Proc. Natl. Acad. Sci. U S A 112, 13675–13680.

Barr, J.J. (2017). A bacteriophages journey through the human body. Immunol. Rev. 279, 106–122.

Bodner, K., Melkonian, A.L., Barth, A.I.M., Kudo, T., Tanouchi, Y., and Covert, M.W. (2020). Engineered fluorescent E. coli lysogens allow live-cell imaging of functional prophage induction triggered inside macrophages. Cell Syst. 10, 254–264.e9.

Bonilla, N., Rojas, M.I., Netto Flores Cruz, G., Hung, S.H., Rohwer, F., and Barr, J.J. (2016). 'Phage on tap–a quick and efficient protocol for the preparation of bacteriophage laboratory stocks'. PeerJ 4, e2261.

Breitbart, M., Hewson, I., Felts, B., Mahaffy, J.M., Nulton, J., Salamon, P., and Rohwer, F. (2003). Metagenomic analyses of an uncultured viral community from human feces. J. Bacteriol. 185, 6220–6223.

Canton, J. (2018). Macropinocytosis: new insights into its underappreciated role in innate immune cell surveillance. Front. Immunol. 9, 2286.

Carroll-Portillo, A., and Lin, H.C. (2019). Bacteriophage and the innate immune system: access and signaling. Microorganisms 7, 1–11.

Chin, W.H., and Barr, J.J. (2019). Phage Research in "Organ-on-chip" Devices. Microbiol. Aust. 28–32.

Clokie, M.R., Millard, A.D., Letarov, A.V., and Heaphy, S. (2011). Phages in nature. Bacteriophage 1, 31–45.

Dabrowska, K., Switała-Jelen, K., Opolski, A., Weber-Dabrowska, B., and Gorski, A. (2005). Bacteriophage penetration in vertebrates. J. Appl. Microbiol. 98, 7–13.

Dąbrowska, K. (2019). Phage therapy: what factors shape phage pharmacokinetics and bioavailability? Systematic and critical review. Med. Res. Rev. 39, 2000–2025.

Dąbrowska, K., and Abedon, S.T. (2019). Pharmacologically aware phage therapy: pharmacodynamic and pharmacokinetic obstacles to phage antibacterial action in animal and human bodies. Microbiol. Mol. Biol. Rev. 83, 1–25.

Davies, P.F., Spaan, J.A., and Krams, R. (2005). Shear Stress Biology of the Endothelium. Ann. Biomed. Eng. 33, 1714–1718.

Dor-On, E., and Solomon, B. (2015). Targeting glioblastoma via intranasal administration of Ff bacteriophages. Front. Microbiol. 6, 530.

Doub, J.B., Ng, V.Y., Johnson, A.J., Slomka, M., Fackler, J., Horne, B., Brownstein, M.J., Henry, M., Malagon, F., and Biswas, B. (2020). Salvage bacteriophage therapy for a chronic MRSA prosthetic joint infection. Antibiotics 9, 241.

Geier, M.R., Attallah, A.F., and Merril, C.R. (1975). Characterization of Escherichia coli bacterial viruses in commercial sera. In Vitro 11, 55–58.

Geier, M.R., Trigg, M.E., and Merril, C.R. (1973). Fate of bacteriophage lambda in Non-immune germ-free mice. Nature *246*, 221–223.

Ghose, C., Ly, M., Schwanemann, L.K., Shin, J.H., Atab, K., Barr, J.J., Little, M., Schooley, R.T., Chopyk, J., and Pride, D.T. (2019). The virome of cerebrospinal fluid: viruses where we once thought there were none. Front. Microbiol. *10*, 2061.

Gogokhia, L., Buhrke, K., Bell, R., Hoffman, B., Brown, D.G., Hanke-Gogokhia, C., Ajami, N.J., Wong, M.C., Ghazaryan, A., Valentine, J.F., et al. (2019). Expansion of bacteriophages is linked to aggravated intestinal inflammation and colitis. Cell Host Microbe *25*, 285–299.e8.

Gordillo Altamirano, F.L., and Barr, J.J. (2019). Phage therapy in the postantibiotic era. Clin. Microbiol. Rev. *32*, 1–25.

Gorski, A., Dabrowska, K., Switala-Jeleń, K., Nowaczyk, M., Weber-Dabrowska, B., Boratynski, J., Wietrzyk, J., and Opolski, A. (2003). New insights into the possible role of bacteriophages in host defense and disease. Med. Immunol. *2*, 2.

Górski, A., Ważna, E., Dąbrowska, B.-W., Dąbrowska, K., Świtała-Jeleń, K., and Międzybrodzki, R. (2006). Bacteriophage translocation. FEMS Immunol. Med. Microbiol. *46*, 313–319.

Han, J., Zern, B.J., Shuvaev, V.V., Davies, P.F., Muro, S., and Muzykantov, V. (2012). Acute and chronic shear stress differently regulate endothelial internalization of nanocarriers targeted to platelet-endothelial cell adhesion molecule-1. ACS Nano *6*, 8824–8836.

Handley, S.A., Thackray, L.B., Zhao, G., Presti, R., Miller, A.D., Droit, L., Abbink, P., Maxfield, L.F., Kambal, A., Duan, E., et al. (2013). pathogenic simian immunodeficiency virus infection is associated with expansion of the enteric virome. Cell *151*, 253–266.

Hatfull, G.F. (2015). Dark matter of the biosphere: the amazing world of bacteriophage diversity. J. Virol. *89*, 8107–8110.

Hildebrand, G.J., and Wolochow, H. (1962). Translocation of bacteriophage across the intestinal wall of the rat. Exp. Biol. Med. *109*, 183–185.

Hodyra-Stefaniak, K., Miernikiewicz, P., Drapała, J., Drab, M., Jończyk-Matysiak, E., Lecion, D., Kaźmierczak, Z., Beta, W., Majewska, J., Harhala, M., et al. (2015). Mammalian Host-Versus-Phage immune response determines phage fate in vivo. Sci. Rep. *5*, 1–13.

Hodyra-Stefaniak, K., Lahutta, K., Majewska, J., Kaźmierczak, Z., Lecion, D., Harhala, M., Kęska, W., Owczarek, B., Jończyk-Matysiak, E., Kłopot, A., et al. (2019). Bacteriophages engineered to display foreign peptides may become short-circulating phages. Microb. Biotechnol. *12*, 730–741.

Hoffmann, M. (1965). Animal experiments on mucosal passage and absorption viraemia of T3 phages after oral, trachéal and rectal administration. Zentralbl. Bakteriol. Orig. *198*, 371–390.

Hosta-Rigau, L., and Städler, B. (2013). Shear stress and its effect on the interaction of myoblast cells with nanosized drug delivery vehicles. Mol. Pharm. *10*, 2707–2712.

Hsiao, I.-L., Gramatke, A.M., Joksimovic, R., Sokolowski, M., Gradzielski, M., and Haase, A. (2014). Size and cell type dependent uptake of silica nanoparticles. J. Nanomed. Nanotechnol. *05*, 248.

Huh, H., Wong, S., St Jean, J., and Slavcev, R. (2019). Bacteriophage interactions with mammalian tissue: therapeutic applications. Adv. Drug Deliv. Rev. *145*, 4–17.

Karimi, M., Mirshekari, H., Moosavi Basri, S.M., Bahrami, S., Moghoofei, M., and Hamblin, M.R. (2016). Bacteriophages and phage-inspired nanocarriers for targeted delivery of therapeutic cargos. Adv. Drug Deliv. Rev. *106*, 45–62.

Keller, R., and Engley, F.B. (1958). Fate of bacteriophage particles introduced into mice by various routes. Exp. Biol. Med. *98*, 577–580.

Kellermayer, M.S.Z., Vörös, Z., Csík, G., and Herényi, L. (2018). Forced phage uncorking: viral DNA ejection triggered by a mechanically sensitive switch. Nanoscale *10*, 1898.

Kerr, M.C., and Teasdale, R.D. (2009). Defining macropinocytosis. Traffic *10*, 364–371.

Kim, H.J., Huh, D., Hamilton, G., and Ingber, D.E. (2012). Human gut-on-a-chip inhabited by microbial flora that experiences intestinal peristalsis-like motions and flow. R. Soc. Chem. *12*, 2165–2174.

Kim, H.J., Li, H., Collins, J.J., and Ingber, D.E. (2016). Contributions of microbiome and mechanical deformation to intestinal bacterial overgrowth and inflammation in a human gut-on-a-chip. Proc. Natl. Acad. Sci. U S A *113*, E7–E15.

Kim, L., Toh, Y.C., Voldman, J., and Yu, H. (2007). A practical guide to microfluidic perfusion culture of adherent mammalian cells. Lab Chip *7*, 681–694.

Kutter, E., De Vos, D., Gvasalia, G., Alavidze, Z., Gogokhia, L., Kuhl, S., and Abedon, S.T. (2010). Phage therapy in clinical practice: treatment of human infections. Curr. Pharm. Biotechnol. *11*, 69–86.

Lehti, T.A., Pajunen, M.I., Skog, M.S., and Finne, J. (2017). Internalization of a polysialic acid-binding Escherichia coli bacteriophage into eukaryotic neuroblastoma cells. Nat. Commun. *8*, 1915.

Lin, Y.W., Chang, R.Y., Rao, G.G., Jermain, B., Han, M.L., Zhao, J.X., Chen, K., Wang, J.P., Barr, J.J., Schooley, R.T., et al. (2020). Pharmacokinetics/pharmacodynamics of antipseudomonal bacteriophage therapy in rats: a Proof-of-Concept study. Clin. Microbiol. Infect. *26* (9), 1229–1235.

Loc-Carrillo, C., and Abedon, S.T. (2011). Pros and cons of phage therapy. Bacteriophage *1* (2), 111–114.

Lu, F., Wu, S.H., Hung, Y., and Mou, C.Y. (2009). Size effect on cell uptake in well-suspended, uniform mesoporous silica nanoparticles. Small 5, 1408–1413.

Manrique, P., Bolduc, B., Walk, S.T., van der Oost, J., de Vos, W.M., and Young, M.J. (2016). Healthy human gut phageome. Proc. Natl. Acad. Sci. U S A *113*, 10400–10405.

Matsuzaki, S., and Uchiyama, J. (2019). Phage pharmacokinetics: relationship with administration route. In Phage Therapy: A Practical Approach, A. Górski, R. Międzybrodzki, and J. Borysowski, eds. (Springer), pp. 43–57.

McQuin, C., Goodman, A., Chernyshev, V., Kamentsky, L., Cimini, B.A., Karhohs, K.W., Doan, M., Ding, L., Rafelski, S.M., Thirstrup, D., et al. (2018). CellProfiler 3.0: next-generation image processing for biology. PLoS Biol. *16*, e2005970.

Merril, C.R., Biswas, B., Carlton, R., Jensen, N.C., Creed, G.J., Zullo, S., and Adhya, S. (1996). Long-circulating bacteriophage as antibacterial agents. Proc. Natl. Acad. Sci. U S A *93*, 3188–3192.

Merril, C.R., Scholl, D., and Adhya, S.L. (2003). The prospect for bacteriophage therapy in Western medicine. Nat. Rev. Drug Discov. *2*, 489–497.

Międzybrodzki, R., Kłak, M., Jończyk-Matysiak, E., Bubak, B., Wójcik, A., Kaszowska, M., Weber-Dąbrowska, B., Lobocka, M., and Górski, A. (2017). Means to facilitate the overcoming of gastric juice barrier by a therapeutic staphylococcal bacteriophage A5/80. Front. Microbiol. *8*, 1–11.

Navabi, N., McGuckin, M.A., and Linden, S.K. (2013). Gastrointestinal cell lines form polarized epithelia with an adherent mucus layer when cultured in semi-wet interfaces with mechanical stimulation. PLoS One 8, e68761.

Nguyen, S., Baker, K., Padman, B.S., Patwa, R., Dunstan, R.A., Weston, T.A., Schlosser, K., Bailey, B., Lithgow, T., Lazarou, M., et al. (2017). Bacteriophage transcytosis provides a mechanism to cross epithelial cell layers. mBio *8*, e01874-17.

Nilsson, A.S. (2014). Phage therapy-constraints and possibilities. Ups J. Med. Sci. *119*, 192–198.

Park, J.Y., White, J.B., Walker, N., Kuo, C.H., Cha, W., Meyerhoff, M.E., and Takayama, S. (2011). Responses of endothelial cells to extremely slow flows. Biomicrofluidics 5, 22211.

Payne, R.J.H., and Jansen, V.A.A. (2000). Phage therapy: the peculiar kinetics of self-replicating pharmaceuticals. Clin. Pharmacol. Ther. *68*, 225–230.

Payne, R.J., and Jansen, V.A. (2001). Understanding bacteriophage therapy as a density-dependent kinetic process. J. Theor. Biol. *208*, 37–48.

Rohwer, F. (2003). Global phage diversity. Cell *113*, 141.

Rohwer, F., and Segall, A.M. (2015). In retrospect: a century of phage lessons. Nature *528*, 46–48.

Schooley, R.T., Biswas, B., Gill, J.J., Hernandez-Morales, A., Lancaster, J., Lessor, L., Barr, J.J., Reed, S.L., Rohwer, F., Benler, S., et al. (2017). Development and use of personalized bacteriophage-based therapeutic cocktails to treat a patient with a disseminated resistant Acinetobacter baumannii infection. Antimicrob. Agents Chemother. *61*, 1–14.

Sender, R., Fuchs, S., and Milo, R. (2016). Are we really vastly outnumbered? revisiting the ratio of bacterial to host Cells in humans. Cell *164*, 337–340.

Shkoporov, A.N., and Hill, C. (2019). Bacteriophages of the human gut: the "known unknown" of the microbiome. Cell Host Microbe *25*, 195–209.

Son, Y. (2007). Determination of shear viscosity and shear rate from pressure drop and flow rate relationship in a rectangular channel. Polymer *48*, 632–637.

Srivastava, A.S., Chauhan, D.P., and Carrier, E. (2004). In utero detection of T7 phage after systemic administration to pregnant mice. BioTechniques *37*, 81–83.

Swanson, J.A., and Watts, C. (1995). Macropinocytosis. Trends Cell Biol. *5*, 424–428.

Sweere, J.M., Van Belleghem, J.D., Ishak, H., Bach, M.S., Popescu, M., Sunkari, V., Kaber, G., Manasherob, R., Suh, G.A., Cao, X., et al. (2019). Bacteriophage trigger antiviral immunity and prevent clearance of bacterial infection. Science *363*, eaat9691.

Talman, L., Agmon, E., Peirce, S.M., and Covert, M.W. (2019). Multiscale models of infection. Curr. Opin. Biomed. Eng. *11*, 102–108.

Tao, P., Mahalingam, M., Marasa, B.S., Zhang, Z., Chopra, A.K., and Rao, V.B. (2013). In vitro and in vivo delivery of genes and proteins using the bacteriophage T4 DNA packaging machine. Proc. Natl. Acad. Sci. U S A *110*, 5846–5851.

Thuenauer, R., Rodriguez-Boulan, E., and Römer, W. (2014). Microfluidic approaches for epithelial cell layer culture and characterisation. Analyst *139*, 3206–3218.

Van Belleghem, J.D., Dąbrowska, K., Vaneechoutte, M., Barr, J.J., and Bollyky, P.L. (2019). Interactions between bacteriophage, bacteria, and the mammalian immune system. Viruses *11*, 10.

Wang, C., Lu, H., and Schwartz, M.A. (2012). A novel in vitro flow system for changing flow direction on endothelial cells. J. Biomech. *45*, 1212–1218.

Wang, H., and Song, M. (2011). Ckmeans.1d.dp: optimal k-means clustering in one dimension by dynamic programming. R. J. *3*, 29–33.

Yin Win, K., and Feng, S.S. (2005). Effects of particle size and surface coating on cellular uptake of polymeric nanoparticles for oral delivery of anticancer drugs. Biomaterials *26*, 2713–2722.

Yum, K., Hong, S.G., Healy, K.E., and Lee, L.P. (2014). Physiologically relevant organs on chips. Biotechnol. J. *9*, 16–27.

Zhu, J., Liao, L., Zhu, L., Zhang, P., Guo, K., Kong, J., Ji, C., and Liu, B. (2013). Size-dependent cellular uptake efficiency, mechanism, and cytotoxicity of silica nanoparticles toward HeLa cells. Talanta *107*, 408–415.

Supplemental information

Bacteriophage uptake by mammalian

cell layers represents a potential

sink that may impact phage therapy

Marion C. Bichet, Wai Hoe Chin, William Richards, Yu-Wei Lin, Laura Avellaneda-Franco, Catherine A. Hernandez, Arianna Oddo, Oleksandr Chernyavskiy, Volker Hilsenstein, Adrian Neild, Jian Li, Nicolas Hans Voelcker, Ruzeen Patwa, and Jeremy J. Barr

1
2
3 **Figure S1. Clustering of cell lines**, related to Figure 1. Clustering was performed using the dynamic programming
4 algorithm in the R package Ckmeans.1d.dp. The given number of clusters was three shown here in the X axis (1 –
5 low uptake, 2 – intermediate uptake and 3 – high uptake) and the percentage of uptake in Y axis. Each colour
6 represents one of the cell lines tested.
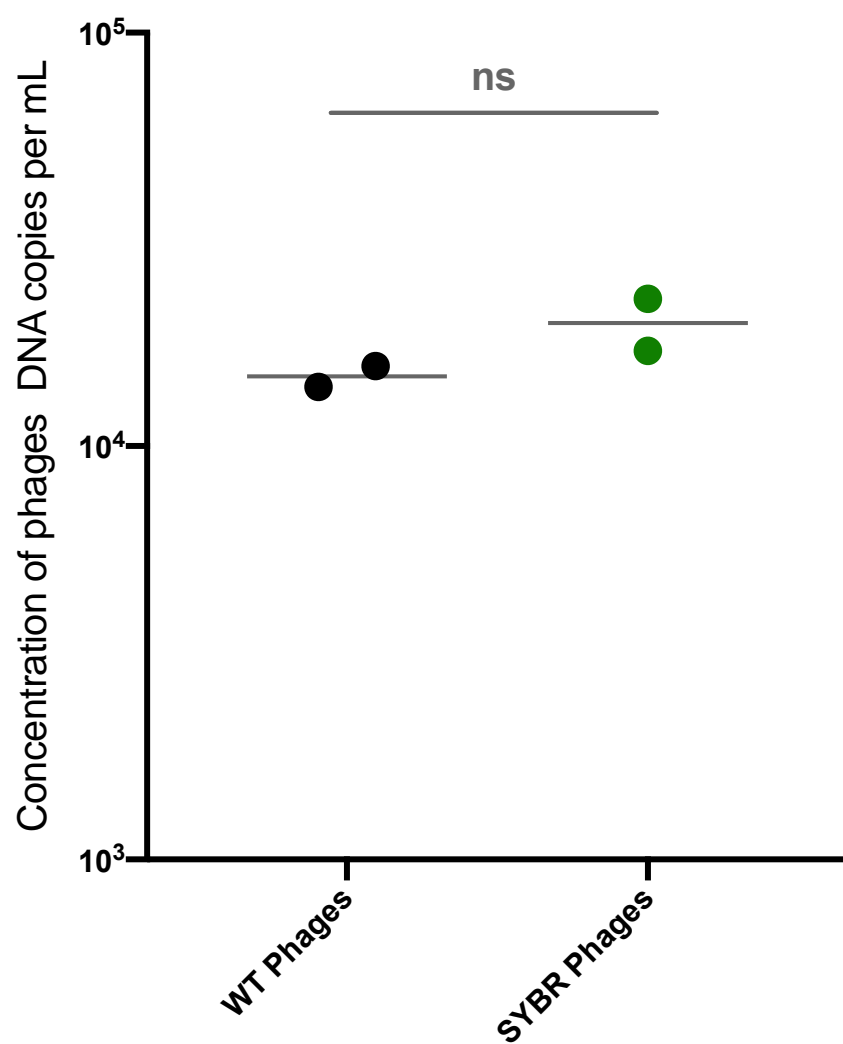
7
8   **Figure S2. SYBR labelled phages rate of uptake compared to non-labelled phages,** related to Figure 1. T4
9   phages labelled and non-labelled were applied on a confluent cell layer of A549 cells for 18 hours. The cells
10 were then washed with DPBS and lysed for analysis using ddPCR. In the Y axis, the phages DNA copies. P-values
11 calculated from a one-way unpaired t-test (ns: non-significant).

a

2.36 cm
1.3 cm
0.5 mm
Depth: 0.35 mm
Diameter: 2.0 mm

b

c

Microfluidic chip
Cell culture media
INFUSE Syringe pump
Waste bottle
Cover slip
Inverted confocal microscope
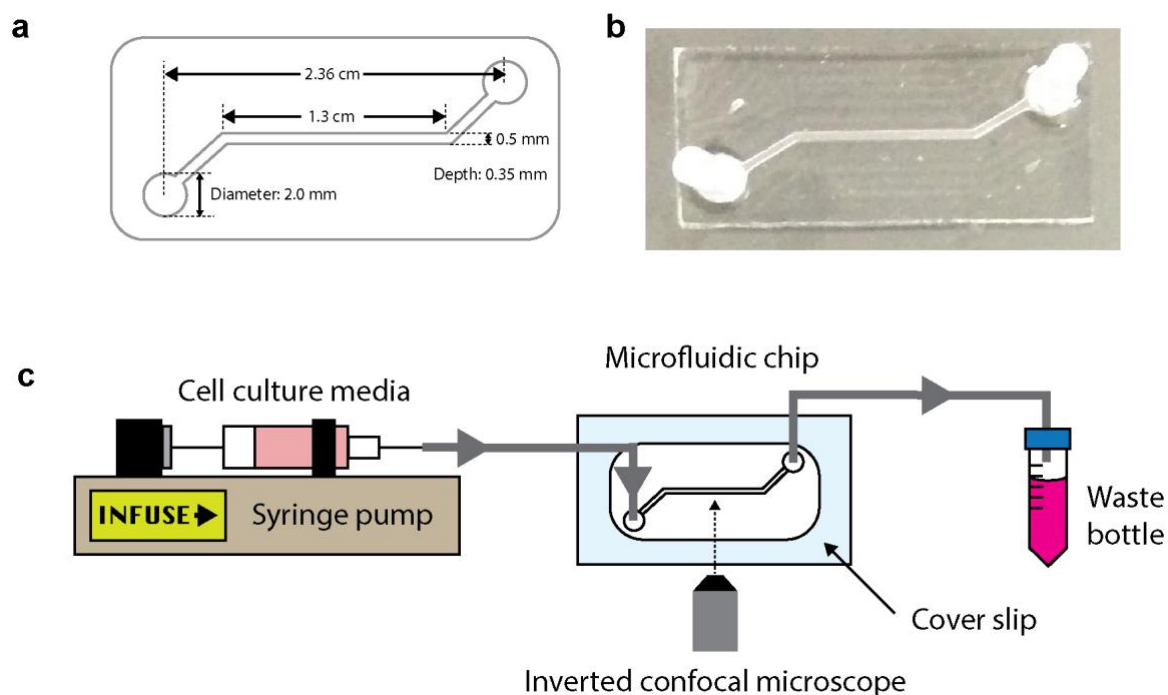
Figure S3. Microfluidic device and set-up for phage transcytosis experiment in flow conditions, related to Figure 3. **(a)** Chip channel dimensions, **(b)** the actual device picture. The chip was fabricated using PDMS and irreversibly bonded onto a glass cover slip using plasma. **(c)** Experimental set-up schematic for transcytosis experiment on flow. After inoculating the device with phages, the cell layer within the microfluidic chip was maintained under flow with egressing fluid collected as waste. Phage and cell layer behaviour were monitored and recorded via an inverted confocal microscope.
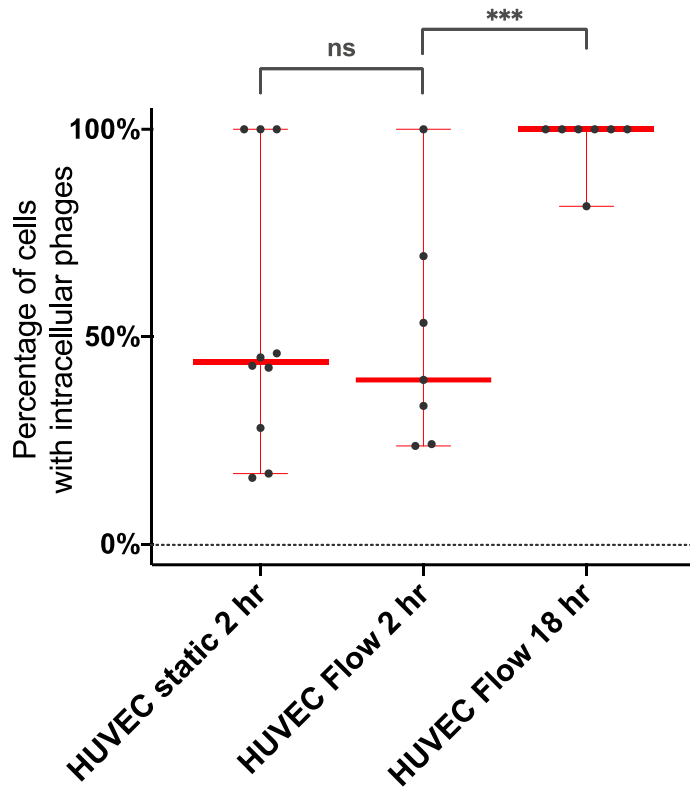
19
20
21 **Figure S4. Intracellular phages under flow conditions**, related to Figure 3. Percentage of HUVEC cells containing
22 intracellular phages at the two-hour time point under static conditions and the two time points under flow condition
23 of 0.1 dyne/cm², two hours and 18 hours. Scatter plots show medians of percentage of cells with intracellular
24 phages; error bars represent 95% confidence intervals; each dot represents one Field of View (FOV). (static, n =
25 10; Flow 2 hr, n = 7; Flow 18 hours, n = 7). P-values calculated from a one-way unpaired t-test (P < 0.001: ***;
26 ns: non-significant).
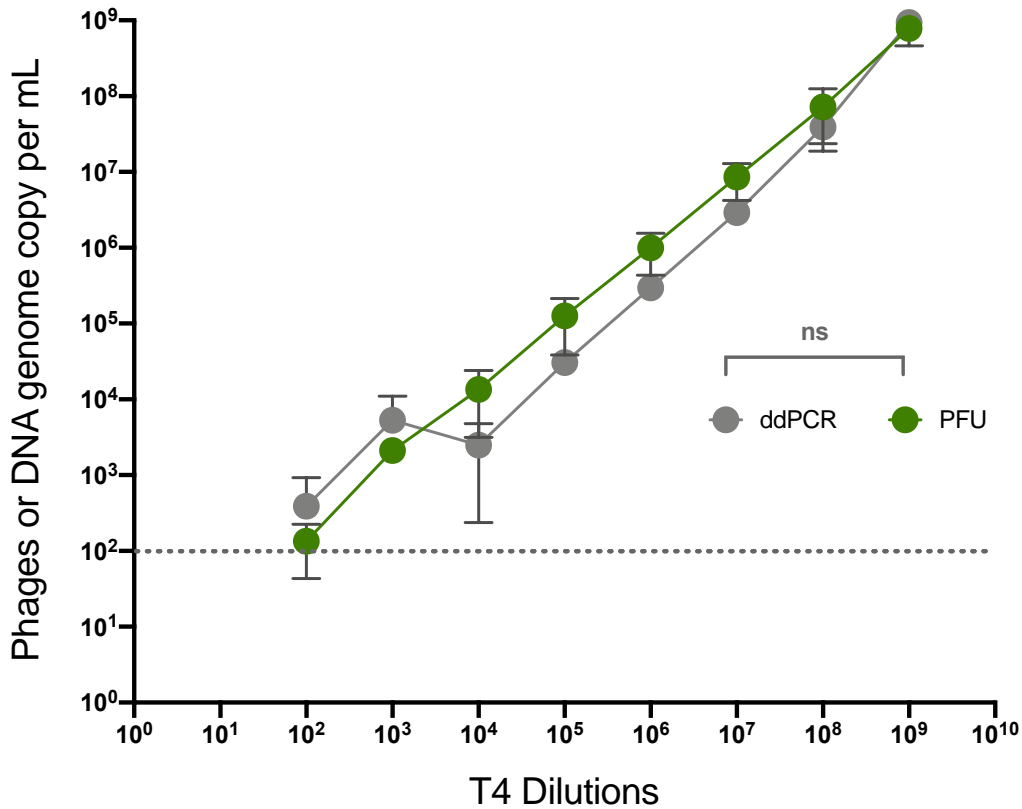
27
28

29 **Figure S5. Dilution series of T4 phage stock using PFU and ddPCR techniques,** related to Figure 5. X axis
30 representing the dilution of the phage stock, in the Y axis the concentrations obtained with PFU or ddPCR in Phages
31 or DNA genome copy per ml respectively. Shown in green line the PFU results and in grey the ddPCR results. Limit
32 of detection is represented by the grey dotted line. P values calculated from paired T-test (ns: non-significant).
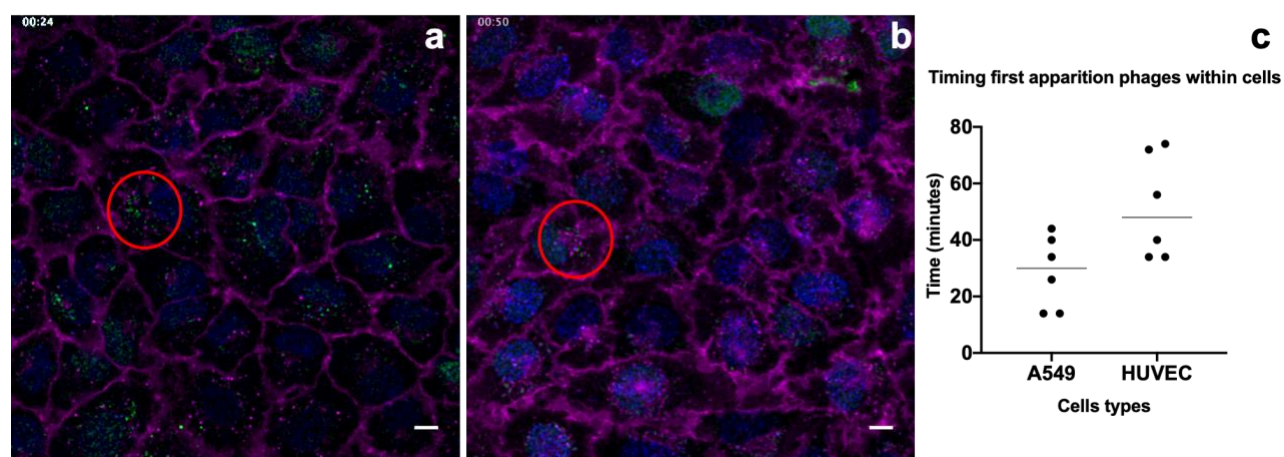
Figure S6. Time of first phage detection inside of cells, related to Figure 5. T4 phages were applied to **(a)** A549 cell layer or **(b)** HUVEC cell layer and incubated for two hours on a μ-Slide 8 well glass bottom slide on a microscope stage with temperature and CO_2 control. One image was acquired every two minutes on an inverted Leica SP8 confocal microscope with HC PL APO 63x/1.40 CS2 oil immersion objective. A hybrid detector (HyD) was used in sequential mode to visualise phage DNA. Cells were stained with nucleus stain, Hoescht 33342 (blue), plasma membrane stain, CellMask (magenta) and T4 phages labelled with DNA-complexing stain, SYBR-Gold (green). Scale bar: 10 μm; Timing: hours:minutes. The red circle represents the first detection of phages DNA within cells at 24 minutes for A549 cells and 50 minutes for HUVEC cells. **(c)** Graph representing the first time when phages appear within the cells in A549 and HUVEC cells in X axis with timing in minutes on the Y axis. Aligned dot plot with the median represented (*n* = 5 for A549 cells; *n* = 6 for HUVEC cells).
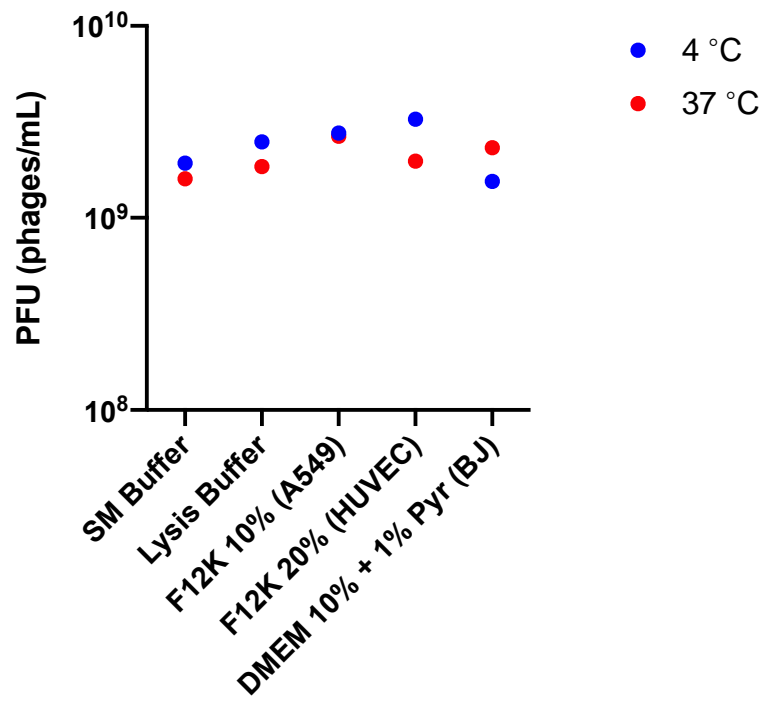
45
46 **Figure S7**. **Concentrations of T4 phage stock using PFU techniques,** related to Figure 5. X axis representing the
47 different media of incubation: stocking media (SM Buffer), the lysis buffer used to lyse the cells and collect the
48 intracellular phages, and the three spent cell culture media used to grow A549, HUVEC or BJ cells. The spent cell
49 culture media was collected after two days of cells growth before being used in this control. In the Y axis the
50 concentrations obtained with PFU in phages/ml. Shown in blue dots the results at 4 °C and in red dots the results
51 at 37 °C. Non-significant P values calculated from one-way ANOVA.

52
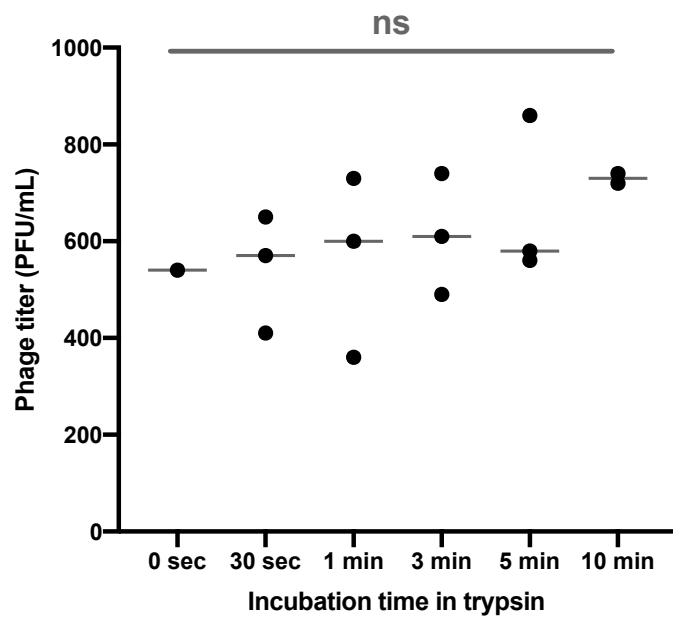
53
54 **Figure S8. Concentrations of T4 phage incubated with 0.5% Trypsin at different incubation times and at 37**
55 **°C**, related to Figure 5. X axis representing the different time of incubation zero to ten minutes. In the Y axis the
56 concentrations obtained with PFU in phages/ml. Aligned dot plot with the median represented ($n = 1$ for 0 minutes;
57 $n = 3$ for 30 sec, 1 min, 3 min and 5 min; $n = 2$ for 10 min). Non-significant P values calculated from one-way
58 ANOVA.

59
60

Table S1. Shear stress calculation, related to Figure 3.

	Constant	μ: Viscosity of media at 37 °C (mPa·s)	Q: flow rate (m³/s)	W: channel width (m)	H: channel height (m)	T: sheer stress (dyne/cm²)
Values	6	0.78	1.33×10^{-10}	5×10^{-4}	3.5×10^{-4}	$\tau = \dfrac{6\mu Q}{WH^2}$

61
62
63

Table S2. Primers and probe DNA sequences for gp23 ddPCR assay, related to Figure 5.

Primers/probes	Sequences	Vendor
Primer gp23 Forward	5'-CTGCAGGTCAGACTTCTG-3'	Micromon
Primer gp23 Reverse	5'-CATCGGCTGAACACCAC-3'	Micromon
Probe gp23	5'-**56-FAM**/ACTCAGATT/**ZEN**/GGCCCAGCTGTT/**3IABkFQ**/-3'	Integrated DNA Technology (IDT)

64
65
66

Table S3. PCR mix for gp23 ddPCR assay, related to Figure 5.

67

	For one reaction (µl)	For 8 reactions (µl)
Super Mix for Probes	10	80
Forward gp23 Primer 10 µM	1.8	14.4
Reverse gp23 Primer 10 µM	1.8	14.4
Gp23 probe 20X	1	8
Water	5.4	43.2
Sample	2	-
Total	22	20 mix + 2 µl sample

68
69

Table S4. Thermal cycling conditions for gp23 ddPCR assay, related to Figure 5.

70

Cycling steps	Time (hr:min:sec)	Temperatures (°C)	Number of cycles
Enzyme activation	00:10:00	95	1
Denaturation	00:00:30	94	40
Annealing	00:01:30	55	40
Extension	00:00:30	72	40
Enzyme deactivation	00:10:00	98	1
Hold	∞	4	1

71
72

Tables S5. Calculation for math model and constants used, related to Figure 6.

73
74

Calculation of the first order constant:

75
76

$$\frac{d[ddPCR]}{dt} = k[ddPCR]$$

77
78
79

$$k = \frac{\ln[ddPCR_o] - \ln[ddPCR]}{t}$$

80

$[ddPCR]$	*phage conc. in central compartment*
$[ddPCR_o]$	*initial phage conc. administered*
t	*elapsed time*
k	*rate constant*
$[ddPCR_o]$ at t:0 (DNA genome copies/mL)	1000000000
$[ddPCR]$ at t:30 seconds (DNA genome copies/mL) *	3392
$[ddPCR]$ at t:18 hours (DNA genome copies/mL) *	363073

81
*Geometric mean of ddPCR data combined between each replicates and cells lines
82

83 Constants used in the model:
84

Data from	Lin et al. 2020
Central volume of distribution (mL/rat)	111
Maximum Elimination rate (PFU/h/rat)	43900000000
Peripheral volume of distribution 1 (mL/rat)	128
Peripheral volume of distribution 2 (mL/rat)	180
Intercompartmental clearance 1 (mL/h/rat)	30.4
Intercompartmental clearance 2 (mL/h/rat)	538
50% of the maximal elimination rate (PFU/mL/rat)	16400000
Dosing time	1
Number of rats per simulation	1
Simulation time (h)	50
Integration step	0.001
Phage initial dose (PFU/mL)	1000000000
First-order inactivation constant t:0 (1/h/rat)	0
First-order inactivation constant t:30 seconds (1/h/rat)	1511
First-order inactivation constant t:18 hours (1/h/rat)	0.44
Formula used to plot the graph in Fig. 6B	DV = log10(CENT/VC + 0.0001)

85

86 **Transparent methods**
87   **Bacterial stocks and phage stocks.** The bacterial strains used in this study, *Escherichia coli B* strain HER
88 1024 and *E. coli B* strain W3350, were cultured in lysogeny broth (LB) media (10 g tryptone, 5 g yeast extract,
89 10 g NaCl, in 1 litre of distilled water [dH$_2$O]) at 37 °C shaking overnight and used to propagate and titre phages
90 T4, T3 and lambda supplemented with 10 mM CaCl$_2$ and MgSO$_4$. Phages T4, T3 and lambda were cleaned and
91 purified using the Phage on Tap protocol (PoT) (Bonilla *et al.*, 2016) and titred up to a concentration of
92 approximately 10^{10} phages/ml. After purification, phages were stored in a final solution of SM Buffer (2.0 g
93 MgSO$_4$·7H$_2$O, 5.8 g NaCl, 50 ml of 1M Tris-HCl pH 7.4, dissolve in 1 litre of dH$_2$O) at 4 °C.
94   **Endotoxin removal.** For each of the phage samples, endotoxin removal protocol was followed from the
95 Phage on Tap (PoT) protocol (Bonilla *et al.*, 2016). Phages lysates were cleaned four times with octanol to remove
96 endotoxins from the lysate and went from 5734 EU/ml, to 167 EU/ml in a phages stock solution at 10^{11} phages/ml.
97 Only 10^9 phages/ml were used in the experiment bringing the endotoxin levels to ~1 EU/ml not including the
98 further dilutions within the cell media. The levels of endotoxins applied to the cells were non-significant in regards
99 to phage therapy use.
100   **Cell line stocks.** Seven cell lines were used in this study, all grown at 37 °C and 5% CO$_2$ and
101 supplemented with 1% penicillin-streptomycin (Life Technologies Australia Pty. Ltd) A549 cells were grown in Ham's
102 F-12K (Kaighn's) (also called F12-K)) (Life Technologies Australia Pty. Ltd) media with 10% Fetal Bovine Serum
103 (FBS) (Life Technologies Australia Pty. Ltd), HUVECs were grown in F12-K media with 20% FBS, HeLa and HT-29
104 cells were both grown in Dulbecco's Modified Eagle Medium (DMEM) (Life Technologies Australia Pty. Ltd)
105 supplemented with 10% FBS, MDCK-I cells were grown in Modified Eagle Medium (MEM) (Life Technologies
106 Australia Pty. Ltd) with 10% FBS, BJ cells were grown in DMEM media with 10% FBS and 1% sodium pyruvate
107 (Sigma-Aldrich, Australia) and finally the suspension of THP-1 cells were maintained in Roswell Park Memorial
108 Institute (RPMI) 1640 media (Life Technologies Australia Pty. Ltd) with 10% FBS. For differentiation, phorbol 12-
109 myristate 13-acetate (PMA) (Sigma-Aldrich, Australia) was added to a final concentration of 25 mM and incubated
110 for 48 hours. After incubation PMA supplemented media was removed and cells were further grown in PMA free
111 media for 24 hours to obtain differentiated macrophages. These differentiated cells were stable for up to one
112 week.
113   **Confocal microscopy.** For confocal microscopy experiment, cells were seeded in an IBIDI μ-Slide 8-well
114 glass-bottom slide (DKSH Australia Pty. Ltd) and grown to 80-90% confluency for acquisition. Cells were treated
115 for 20 min with the respective culture media for each cell line with 5% Hoechst 33342 stain, excitation/emission
116 361/497 nm (Life Technologies Australia Pty. Ltd) and 1% CellMask deep red plasma membrane stain,
117 excitation/emission 649/666 nm (Life Technologies Australia Pty. Ltd). After incubation cells were washed three
118 times with Dulbecco's phosphate-buffered saline (DPBS) 1× and then left in Hank's Balanced Salt Solution (HBSS)
119 with 1% FBS until acquisition. Purified phages were labelled with 1% SYBR-Gold, excitation/emission 495/537
120 nm (Life Technologies Australia Pty. Ltd) for one hour in the dark at 4 °C, followed by three washes with HBSS in
121 Amicon-Ultra4 centrifugal unit 100-kDa membrane (Merck Pty. Ltd) to remove excess of stain. The washed phages
122 were resuspended in a final volume of 1 ml in HBSS media. From a 10^9 phage per ml solution, we added 200 μl
123 in each well to the cells under the microscope right before the start of the acquisition. The effect of SYBR-Gold on
124 phage activity was tested using ddPCR by comparing labelled and un-labelled phages, with no significant effect
125 detected (Fig. S2). Cells were imaged with HC PL APO 63x/1.40 Oil CS2 oil immersion objective by Leica SP8
126 confocal microscope on inverted stand with a hybrid detector (HyD) in real time. Excitation used for Hoechst 33342
127 (blue), SYBR-Gold and CellMask deep red was 405, 488 and 638 nm; corresponding emission was recorder at
128 412-462, 508-545 and 648-694 nm detection ranges respectively. HyD detector was used in sequential mode to
129 detect the phages, it increases the sensitivity of detection by acquiring the same image multiple times and
130 accumulating the fluorescence signal. All live cell imaging experiments were completed in triplicate (three fields
131 of view in each session). One image was acquired every 2 minutes for 2 hours. Each field of view was hand-picked
132 depending on the cell confluency and success of staining. Videos were created through post-processing using the
133 FIJI software version 2.0.0-rc-68/1.52f (Schindelin *et al.*, 2012). First, the three channels acquired were merged
134 and processed with a Gaussian Blur filter of 0.8. Second, each channel brightness and contrast were enhanced for
135 printing quality. Finally, the time and scale were added to the final movie saved in 12 fps.
136   **Quantification of phages in live cell imaging.** For each live cell experiment, we quantified cells that
137 contained intracellular green fluorescence as indicative of SYBR-Gold labelled phages. Live cell images were
138 acquired every ten minutes were quantified by manual counting the total number of cells in the field of view and
139 the number of cells with intracellular phages to calculate the percentage of cells containing intracellular phages.
140 Results were plotted using the GraphPad Prism version 8.4.2 for macOS GraphPad Software, San Diego,
141 California USA, www.graphpad.com, to show uptake of phages over time.
142   **Clustering analysis.** Univariate clustering was performed using the dynamic programming algorithm in
143 the R package Ckmeans.1d.dp (Wang and Song, 2011).
144   **Flow conditions in microfluidic chip.** A chip mould with 500 μm wide, 350 μm high and 1.3 cm long
145 channels was designed using SolidWorks® 2017. The moulds were 3D-printed using Object Eden360V (Stratasys,
146 USA) with a manufacturer-provided polymer FC720 and surface-salinised in a vacuum desiccator overnight with
147 20 μl trichloro(1*H*,1*H*,2*H*,2*H*-perfluorooctyl)silane (Sigma-Aldrich, USA). The microfluidic chips were manufactured
148 via soft-lithography, by casting a 10:1 mixture of Sylgard 184 PDMS and its curing agent (Dowsil, USA)

149 respectively, onto the moulds and were cured at 90 °C until completely solidified (~2 hours). The chips were then
150 cut with a surgical knife, gently peeled off, trimmed and their inlet and outlet were punched with 2 mm biopsy
151 punchers (ProSciTech, Australia). Subsequently, the chips were washed in pentane and acetone to remove residual
152 uncured PDMS. Atmospheric plasma generated at 0.65 Torr with high radio frequency was used to bound the
153 PDMS chip to a glass cover slip No. 1.5H (0.170 mm ± 0.005 mm thickness) optimised for confocal microscopy
154 (Marienfeld), for 20 seconds. The microchannel of the assembled microfluidic device were washed with ethanol
155 (80% v/v)-sterilised, UV-sterilised and pre-treated with 1:50 MaxGel^{TM} ECM (Sigma-Aldrich) in cold F12-K media
156 for 2 hours at 37 °C and 5% CO_2. The microchannel was then washed with F12-K media to remove residual ECM.
157 Schematic and picture of the microdevice is included in Fig. S3. The channel was seeded with 10 μl of HUVECs at
158 a concentration of 5×10^5 cells/ml, which were carefully pipetted through the in port. The seeded chip was
159 incubated statically for 12 hours to allow cell attachment at 37 °C and 5% CO_2. This was followed by perfusing
160 the attached cells with complete media for 24 hours at 0.66 μl/min flow rate to establish a confluent cell layer.
161 The cells were then perfused with cell culture media supplemented with 20% of FBS for another 24 hours at 8
162 μl/min to acclimate the cells to the shear stress. Perfusion was mediated by a single-channel syringe pump (New
163 Era Pump Systems, USA) using a 10 ml 21 gauge needled-syringe fitted to Teflon tubes of 1/16" inner diameter
164 and 1/32" outer diameter (Cole-Palmer, USA) that were previously sterilised using ethanol (80% v/v)-sterilised,
165 DPBS and UVs. HUVECs were then stained with nucleus stain, Hoechst 33342 (blue), plasma membrane stain,
166 CellMask (magenta) under static conditions for 20 minutes. T4 phages labelled with DNA-complexing stain, SYBR-
167 Gold (green) were then added to the chip under 8 μl/min flow rate for either 2 or 18 hours. After incubation under
168 flow with the phages, the in and out port of the chips were sealed using sterilized-binder paper clips and the chip
169 placed under the microscope. The images were acquired with HC PL APO 63x/1.40 Oil CS2 oil immersion objective
170 on an inverted Leica SP8 confocal microscope. A hybrid detector (HyD) was used to visualise phage DNA
171 (excitation/emission 495/537 nm), other channels were acquired with conventional PMT detectors for CellMask
172 (excitation/emission 649/666 nm) and for Hoechst 33342 (excitation/emission 361/497 nm).
173   **Image analysis with CellProfiler.** To quantify the fluorescence intensity of SYBR-Gold labelled phages
174 (495 nm wavelength), we used a pipeline created in CellProfiler (McQuin *et al.*, 2018) (see the pipeline used in
175 data SD1), allowing us to measure the pixel grey values as a proxy for fluorescence intensity across the image.
176 First, we segmented regions covered by nuclei by applying the IdentifyPrimaryObjects module to the Hoechst
177 channel image. Second, we defined expanded regions around the nuclei for cytoplasmic measurements using the
178 IdentifySecondaryModule with the parameter Distance-N set to 200. Third, we masked out nuclei regions in the of
179 the nuclei SYBR (phages) channel. This is to exclude fluorescence coming from the cell nuclei due to the leaking of
180 the SYBR dye from the phage capsid to the cell nuclei, which would lead to false positive quantification. Finally,
181 the grey values image intensity in the masked SYBR channel and additional parameters of the secondary objects
182 were measured (Data SD1). Only a single time point at 2 hours at each field of view was used for the analysis.
183 The number of images analysed for each condition varied, as manual quality control was applied to exclude out
184 of focus and non-analysable fields of view.
185   **Intracellular phages.** For the intracellular phages experiment, cells were plated in T25 cm^2 flasks until
186 they reached confluency. For the 18 hours experiment, phages were applied in volumes of 3 ml of media with 10^9
187 phages/ml per flask and incubated overnight at 37 °C and 5% CO_2. The control flasks were incubated with 3 ml
188 of phage-free media. After the 18 hours incubation, control flasks were incubated with the same phage dilution
189 for 30 seconds. The initial dilution for each flask was collected for quantification. Cells were washed three times
190 with 5 ml of $1 \times$ DPBS to remove non-adherent phages. Next, one ml of 0.5% trypsin was added to the flask and
191 incubated at 37 °C and 5% CO_2 for a few minutes. Trypsin was tested to confirm that it did not have any effect
192 on phage activity (Fig. S8). Once cells detached, the cells were resuspended in 5 ml of $1 \times$ DPBS and spun at 1500
193 rpm for three minutes and washed three times with 5 ml $1 \times$ DPBS to remove any non-adherent phages. After the
194 washes, cells were resuspended in 1 ml of lysis buffer (0.5 M EDTA and 1 M Tris at pH 7.5, complete with dH_2O
195 and adjust pH to 8) and left at room temperature for 20 min. After incubation the cells are passed through a 30
196 G syringe three times to ensure complete cell lysis. The lysis was confirmed by looking at the sample under a
197 microscope.
198   **ddPCR setup.** Digital Droplet Polymerase Chain Reaction (ddPCR) was performed following
199 manufacturer's instructions (Bio-Rad, Australia). A 20 μl reaction was assembled with primers, probe, ddPCR
200 Supermix for probe (Bio-Rad, Australia) and sample. The primer and probe sequence and PCR parameters are
201 shown in Table S2 - S4. ddPCR reaction mix was then loaded into eight channel disposable droplet generator
202 cartridge (Bio-Rad, Australia). 70 μl of droplet generation oil was added to each channel and placed in the Bio-
203 Rad QX200 droplet generator. The droplets were transferred into the deep well 96 well plate (Bio-Rad, Australia),
204 using a multichannel pipette. The plate was then sealed using Bio- Rad plate sealer and then placed in a
205 conventional thermocycler and the PCR product was amplified (Table S4). After amplification, the plate was loaded
206 into the droplet reader (Bio-Rad, Australia) to quantify the fluorescent droplets. Analysis of the data was performed
207 using the Poisson distribution with QuantaLife software (Bio-Rad, Australia).
208   **PFU quantification.** The Plaque Forming Unit (PFU) assay was performed using LB agar plates where a
209 thin layer of soft LB agar was mixed with one ml of host bacterial culture and the desired dilution of phages was
210 poured on the agar plate. The plate was incubated over-night at 37 °C before counting the number of plaques

211 formed on the bacterial lawn. The results were calculated in PFU. To obtain the number of inactive phages we
212 subtracted PFU numbers (active phages) from the ddPCR numbers (total number of phages).
213 **Pharmacokinetics model.** A previously developed PK model in healthy rats was utilized to evaluate the
214 impact of phage inactivation on *in vivo* phage disposition (Lin *et al.*, 2020). An additional compartment was
215 incorporated to describe the inactivation and reactivation of phages by the epi- and endothelial cells. The rates
216 of inactivation and reactivation was described by first-order rate constant, KD, and was assumed to be constant
217 over time. The differential equations for phage disposition and inactivation were represented by:
218
219
$$\frac{dA_1(t)}{dt} = -(CL_T + Q_1 + Q_2)\frac{A_1}{V_1}(t) + Q_1\frac{A_3}{V_3}(t) - KD_1A_1(t) + KD_2A_4(t)$$
220
221
$$\frac{dA_2(t)}{dt} = Q_1\frac{A_1}{V_1}(t) - Q_1\frac{A_2}{V_2}(t)$$
222
223
$$\frac{dA_3(t)}{dt} = Q_2\frac{A_1}{V_1}(t) - Q_2\frac{A_3}{V_3}(t)$$
224
225
$$\frac{dA_4(t)}{dt} = KD_1A_1(t) - KD_2A_4(t)$$
226
227
$$CL_T = \frac{V_{max}}{K_m + \frac{A_1}{V_1}}$$
228 where
229 Q_1 = inter-compartmental clearance 1 (ml/h/rat).
230 Q_2 = inter-compartmental clearance 2 (ml/h/rat).
231 V_1 = Volume of distribution of the central compartment (ml/rat).
232 V_2 = Volume of distribution of the peripheral compartment 1 (ml/rat).
233 V_3 = Volume of distribution of the peripheral compartment 2 (ml/rat).
234 K_m = Phage titre that produces 50% of the maximal elimination rate of the system (PFU/ml/rat).
235 V_{max} = Maximum elimination rate (PFU/h/rat).
236 KD_1 = Inactivation rate constant (1/h).
237 KD_2 = Reactivation rate constant (1/h).
238 Deterministic was performed using model-predicted median PK parameters in rats without inter-individual
239 variability and random unexplained variability (Code available in SD2 and SD3 and Table S5). Inactivation rate
240 constant was determined using the ddPCR results as described in table S5. First order for the 30 seconds graph is
241 of 1415 1/h/rat and for the 18 hours the first order is of 0.358 1/h/rat calculated from the ddPCR data.
242 Reactivation rate constant was fixed to 0. Deterministic simulations were performed in R using mrgsolve (version
243 0.10.4) (Bunn and Korpela, 2019; Lin *et al.*, 2020).

244 **References**
245 Schindelin, J. *et al.* (2012) 'Fiji: an open-source platform for biological-image analysis', *Nature Methods*, 9(7).
246